Construction and Building Materials 527 (2026) 146477

Contents lists available at ScienceDirect

Construction and Building Materials

journal homepage: www.elsevier.com/locate/conbuildmat

BOF slag hydration activated by trisodium nitrilotriacetate (Na_3NTA)

Zhihan Jiang [a], Helong Song [b,c,d,*], Xuan Ling [a], Tao Liu [e], Katrin Schollbach [a], H.J.H. Brouwers [a]

[a] Department of the Built Environment, Eindhoven University of Technology, Eindhoven 5600 MB, the Netherlands
[b] Key Laboratory of Coastal Urban Soil-Water Environmental Evolution, Ministry of Ecology and Environment (under construction), Shenzhen University, Shenzhen, 518060, China
[c] State Key Laboratory of Intelligent Geotechnics and Tunnelling (Shenzhen University), Shenzhen, 518060, China
[d] College of Civil and Transportation Engineering, the Underground Polis Academy, Shenzhen University, Shenzhen, 518060, China
[e] Construction Materials and Durability, Department of Environmental and Resource Engineering, Technical University of Denmark, Kgs Lyngby 2800, Denmark

ARTICLE INFO

Keywords:
BOF slag hydration
Nitrilotriacetate (Na_3NTA) activation
Hydration kinetics
Mineral phase evolution
Heavy metal leaching

ABSTRACT

Basic oxygen furnace (BOF) slag exhibits a mineralogy comparable to that of Portland cement, notably containing brownmillerite and belite (C_2S). However, its intrinsic hydraulic reactivity is limited. This work introduces trisodium nitrilotriacetate (Na_3NTA) as a novel activator for BOF slag and systematically evaluates its effects on hydration kinetics, phase evolution, microstructure, mechanical performance, and leaching behavior. Techniques, including isothermal calorimetry, XRD, TG/DTG, FTIR, MIP, and ICP-OES, were applied. Results reveal that Na_3NTA substantially promotes hydration, with no induction period in activated samples. At a dosage of 3.6 wt% Na_3NTA, brownmillerite and C_2S attain hydration degrees of 63.2% and 29.5% within 1 day, respectively (versus 7.6% and near 0% in the control). In activated samples, the hydration assemblage is dominated by hydrogarnet and C–S–H gel, whereas the inactivated reference primarily yields hydrotalcite and C–S–H gel. NTA complexes are rapidly incorporated into the solid matrix at an early age. Moreover, Na_3NTA activation leads to rapid and pronounced improvements in both mechanical performance and pore structure: with 3.6 wt% Na_3NTA usage, a 25.0 MPa compressive strength and a 20.2% porosity are obtained at 7 day, compared with 2.8 MPa and 34.6% for the reference. Hazardous elements, Cr and V, are effectively immobilized in the hydrated solid matrix, with leaching values far below legal thresholds. This research presents a promising approach to valorize BOF slag as a sustainable binder via Na_3NTA activation.

1. Introduction

Basic Oxygen Furnace (BOF) slag is a metallurgical residue formed during the Linz-Donawitz steel-making process [1,2]. The chemical and mineralogical composition of BOF slag varies due to differences in the origin of iron ore, steel-making operational parameters, and cooling conditions. Nevertheless, its primary chemical constituents are well characterized, comprising mainly CaO, Fe_2O_3, SiO_2, MgO, MnO, and Al_2O_3, along with minor components such as TiO_2, V_2O_5, P_2O_5, and Cr_2O_3 [1,2]. The main minerals include dicalcium silicate (C_2S), brownmillerite ($C_2(A,F)$), magnetite (Fe_3O_4), wuestite (RO solid solution of FeO, MgO, MnO, and CaO), and free lime, along with the presence of a small amount of tricalcium silicate (C_3S) in some cases [1–5].

Steel production via the Basic Oxygen Furnace (BOF) method accounts for approximately 71.1% of global crude steel production, totaling around 1345 million tons in 2023 [6]. Consequently, BOF slag is generated in substantial quantities, representing approximately 10–15 wt% of BOF crude steel production [2,7,8]. The large-scale generation and accumulation of BOF slag pose environmental concerns, including land occupation and the potential leaching of heavy metals into the ecosystem [1,2,9–12]. BOF slag has yet to be efficiently recycled and utilized despite its significant volume. For instance, in the construction industry, its primary application is as aggregate in asphalt mixtures, a practice constrained by its susceptibility to volume unsoundness. Additionally, it is used as a supplementary cementitious material in Portland cement systems, albeit at low replacement ratios due to its limited hydraulic reactivity [2,8,12–18].

Despite its current underutilization in the construction industry, BOF

* Corresponding author at:Key Laboratory of Coastal Urban Soil-Water Environmental Evolution, Ministry of Ecology and Environment (under construction), Shenzhen University, Shenzhen, 518060, China.
E-mail address: hlsong@szu.edu.cn (H. Song).

https://doi.org/10.1016/j.conbuildmat.2026.146477
Received 6 February 2026; Received in revised form 27 March 2026; Accepted 23 April 2026
Available online 27 April 2026

slag exhibits significant potential as a high-substitution or even standalone cementitious material due to its mineralogical composition, which resembles that of Portland cement [3,5,19]. This potential utilization could substantially enhance the efficiency of BOF slag recycling. Moreover, given the widespread demand for cement in the construction sector and the heavy reliance of cement production on finite natural mineral resources, integrating BOF slag as a partial or complete replacement for cement presents multiple benefits. In addition to mitigating BOF slag accumulation, such utilization can reduce dependence on depleting mineral reserves and lessen the environmental impact of cement manufacturing, particularly carbon dioxide emissions. It not only aligns with sustainable resource management but also holds considerable promise for advancing environmentally friendly construction practices.

A diverse suite of approaches has been investigated to render BOF slag hydraulically reactive and suitable for use as a cementitious binder. Traditional approaches include applying energy-intensive mechanical comminution to increase the specific surface area and induce lattice disorder in grains, as well as subjecting the material to elevated temperatures or hydrothermal conditions to promote hydration [20–23]. Also, traditional alkali and salt activations were investigated to promote hydration by increasing the pore solution pH or providing additional calcium or aluminium [5,20,24–29]. Additionally, carbonation activation was investigated due to the high pH and alkaline earth metal content within the BOF slag system [30–36]. Although numerous strategies have been proposed, most involve additional processing effort and energy input without achieving a proportionate improvement in mechanical performance. In addition to these methods, activation by small organic ligands (chelators) has recently drawn attention [35–47].

Rather than functioning through increasing solution pH, ligands (chelators) act by transferring lone electron pairs onto the surface metal atoms of undissolved metal (oxide) mineral grains, thus disrupting the (surface) crystal lattice and promoting the dissolution of these minerals [48–53]. The dissolution of BOF slag hydraulically reactive phases is enhanced, thereby facilitating the formation of hydration products. However, the choices of effective ligands remain limited. Against this background, this paper proposes trisodium nitrilotriacetic acid (Na_3NTA), an amino polycarboxylate ligand with high chelating capacity, as an innovative activator [54–57].

As previously discussed, the potential hydration capacity of BOF slag arises from its mineralogical similarity to Portland cement, particularly due to the presence of hydraulically reactive phases such as dicalcium silicate (C_2S) and brownmillerite ($C_2(A,F)$). However, the hydration reactivity of C_2S is inherently limited, contributing minimally to early-stage strength development due to its sluggish reaction kinetics [5,58–61]. This challenge is further exacerbated in BOF slag, where C_2S often contains impurities such as P^{5+} and Fe^{3+}, further diminishing its reactivity [2,62,63]. In contrast, brownmillerite undergoes rapid initial dissolution, akin to calcium aluminate (C_3A) in ordinary Portland cement (OPC) [64,65]. However, its hydration rate declines sharply over time, resulting in a substantially lower overall degree of hydration than that of calcium aluminate [66–68]. This phenomenon is most likely caused by the rapid formation of the iron-based amorphous phase with a high specific surface area around the brownmillerite, which inhibits further mass transport (ion release) [69,70]. The hydration reactivity of brownmillerite in BOF slag is further reduced compared with that in OPC. This reduction is primarily attributed to its elevated Fe content and the additional presence of Ti, which hinders its dissolution and subsequent precipitation into stable hydration products [40,71,72].

The selection of Na_3NTA as a hydration activator is based on its potential to enhance the dissolution and subsequent hydration of the above two key hydraulically reactive phases in BOF slag: impurity-incorporated belite (C_2S) and Fe-rich brownmillerite ($C_2(A,F)$). It is a commercially synthesized tetradentate chelating agent with a strong affinity for a wide range of transition metal ions, particularly divalent and trivalent species, forming stable, soluble complexes [51,52,54,73–80]. Na_3NTA has been widely used in various industries, including cosmetics, pharmaceuticals, water treatment, agriculture, and the food industry as a preservative [54,74–76,81]. In this study, the influence of its dosage on BOF slag hydration was comprehensively examined using various characterization techniques. The early-stage hydration kinetics (within the first seven days) were analyzed using isothermal calorimetry, while the evolution of phase assemblage after 1, 7, and 28 days of hydration was characterized by quantitative X-ray diffraction (QXRD) analysis, supplemented by thermogravimetric (TG/DTG) analysis. Macroscopic mechanical properties were evaluated through compressive strength testing, and microstructural pore characteristics were investigated using mercury intrusion porosimetry (MIP). Additionally, Fourier transform infrared (FTIR) spectroscopy was employed to assess the retention and incorporation of NTA (complexes) within the hydration products. Finally, the heavy metal leaching potential of Na_3NTA-activated BOF slag was evaluated through a one-stage batch leaching test, with elemental concentrations determined by inductively coupled plasma atomic emission spectrometry (ICP-OES).

2. Materials and methods

2.1. Materials

2.1.1. Raw BOF slag

The BOF slag used in the research was sourced from Tata Steel (The Netherlands). Following collection, the slag was pre-crushed into particles smaller than 5.6 mm and stored in a food-grade, airtight polyethylene (PE) container to mitigate carbonation. Subsequently, it was milled to a fine powder using a vibratory disk mill (RS 300 XL, Retsch) as a binder. The particle size distribution (PSD) of the milled BOF slag powder was analyzed using laser diffraction spectroscopy (Mastersizer 2000, Malvern), with the results depicted in Fig. 1. The D10, D50, and D90 values are 1.7, 9.1, and 45.0 μm, respectively. The specific surface area is 310 m^2/kg. The apparent density, measured using a helium pycnometer (AccuPycTM II 1340), is 3.69 g/cm^3. The typical chemical and mineral compositions of the BOF slag, determined by X-ray fluorescence (XRF) analysis (Axios, PANalytical) and XRD analysis (D4 Endeavor, Bruker) tests, respectively, are summarized in Table 1. Mineral quantification was conducted using TOPAS software (V. 5.0, Bruker).

2.1.2. Activator

The activator, Na_3NTA ($C_6H_9NO_6Na_3$, 257.08 g/mol), is the trisodium salt form of (2,2′,2″)-nitrilotriacetic acid [81,82]. Its chemical structure is illustrated in Fig. 2a. Na_3NTA appears as a white to transparent crystalline powder and exhibits exceptionally high solubility (93 g/100 mL at 20 °C) and a high pH (10.5–11.5) in a 1% aqueous solution [81,83]. These properties facilitate solution preparation and

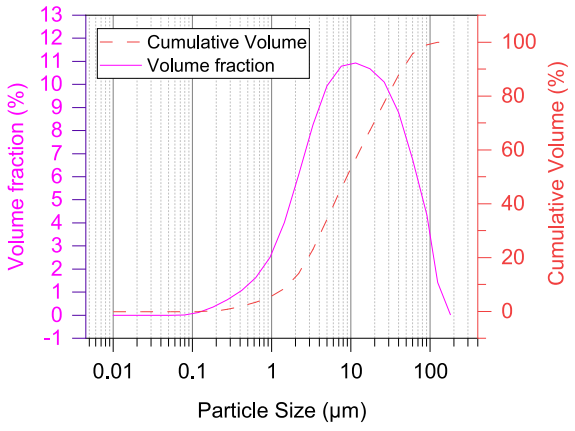

Fig. 1. Particle size distribution of disk-milled BOF slag powder.

Table 1
Chemical and mineralogical composition of milled BOF slag.

Chemical compositions	Content (at%)	Minerals	Content (wt%)
CaO	40.5	Wuestite	21.5
Fe_2O_3	26.5	Magnetite	5.5
SiO_2	14.5	Brownmillerite	14.0
MgO	7.6	C_2S (α' + β)	36.8
MnO	4.5	Lime	0.7
Al_2O_3	1.8	Portlandite	0.6
TiO_2	1.6	Calcite	0.1
V_2O_5	0.9	Amorphous	20.9
P_2O_5	1.6		
Cr_2O_3	0.3		
Na_2O	0.1		
GOI* 1000	1.4		

* Mass gain of ignition (GOI) observed after heating BOF slag to 1000 °C, attributed to the oxidation of metallic oxides, particularly divalent iron.

enhance its effectiveness as an activator in OPC-analogous, alkaline-favored systems. The monohydrate form of Na_3NTA (technical grade, purity 99 +%, Thermo Fisher Scientific) was purchased and used.

It should be noted that an additional ligand, tri-potassium citrate (TPC), was also employed in the hydration kinetics investigation (Section 2.3.1), as a reference activator. TPC is a tricarboxylate, tetradentate ligand (Fig. 2b) that has previously demonstrated efficacy in activating BOF slag hydration [40]. However, its action is predominantly directed toward brownmillerite, with comparatively limited impact on C_2S hydration [40]. Consequently, TPC served as a benchmark against which the performance of Na_3NTA was evaluated. The monohydrate form of TPC (extra pure 99%, Thermo Fisher Scientific) was purchased and used.

2.2. Sample preparation

Paste samples of BOF slag powder mixed with varying concentrations of Na_3NTA solution were made and cured, as summarized in Table 2. The specimen designated as N00, which consisted of BOF slag mixed solely with deionized water, served as the reference. Its water-to-binder (w/b) ratio was determined through preliminary experiments to ensure comparable workability to that of the Na_3NTA-activated samples. The preparation of paste samples followed a systematic procedure. Initially, Na_3NTA powder was dissolved in deionized water, stirred, and allowed to cool. Within 30 s, the Na_3NTA solution or deionized water was added to a steel mixing bowl containing BOF slag powder, followed by 30 s of low-speed stirring. The steel mixing bowl and blade met the EN 196-1 standard [84]. Subsequently, the mixture was stirred at high speed for two minutes to ensure thorough interaction between the BOF slag particles and the Na_3NTA solution or deionized water, resulting in a homogeneous paste. After mixing, the paste was cast into a plastic mold with three prism compartments measuring 4 cm × 4 cm × 16 cm. The mold was then subjected to 15 jolts on a jolting table in accordance with EN 196-1 [84]. To minimize moisture loss, the mold was covered with a transparent plastic film and stored in a standard curing room maintained at 20 ± 1 °C and 95% relative humidity (RH) until the specified curing ages, as detailed in Table 2 [84]. Upon reaching the designated curing age, the plastic film was removed, and the prisms were demolded for subsequent testing and characterization.

2.3. Investigated properties and related methods

Various techniques were employed to characterize the properties of hydrated BOF slag samples and to assess the effects of Na_3NTA comprehensively.

2.3.1. Early-age hydration kinetics

The early-age hydration heat release of samples activated by varying doses of Na_3NTA, as shown in Table 2, was monitored using an isothermal calorimeter (TAM Air, Thermometric). Initially, the raw disk-milled BOF slag powder was placed into pre-labeled glass ampules. Subsequently, Na_3NTA solutions of different concentrations or deionized water were introduced into the respective ampules using a pipette. It is important to note that Na_3NTA solutions were prepared one hour prior to mixing with BOF slag powder to eliminate potential disturbances caused by the initial dissolution of Na_3NTA. After adding the liquid, each ampule was shaken for 60 s on a mini shaker (TopMix FB15024, Fisher Scientific) (as an external stirring procedure) to ensure thorough mixing and homogenization of the paste. The thermostat was pre-set to 20 °C. The exothermic behavior of the samples, including heat flow and cumulative heat release, was continuously recorded over the first seven days of hydration.

An additional sample, C10, was prepared with 1.0 wt% TPC, corresponding to a molar concentration equivalent to 0.9 wt% Na_3NTA. The corresponding mix design is presented in Table 2.

Table 2
Mix design of BOF slag specimens.

Specimen	Water/BOF	Na_3NTA (wt% to BOF slag, molar concentration (mM))	Age (d)
N00	0.24	0.0, 0.0	1
			7
			28
N09	0.20	0.9, 163.5	1
			7
			28
N18	0.20	1.8, 327	1
			7
			28
N36	0.20	3.6, 654	1
			7
			28
C10	0.20	1.0, 163.5	*

* For the calorimetry test throughout the first 7 days of hydration.

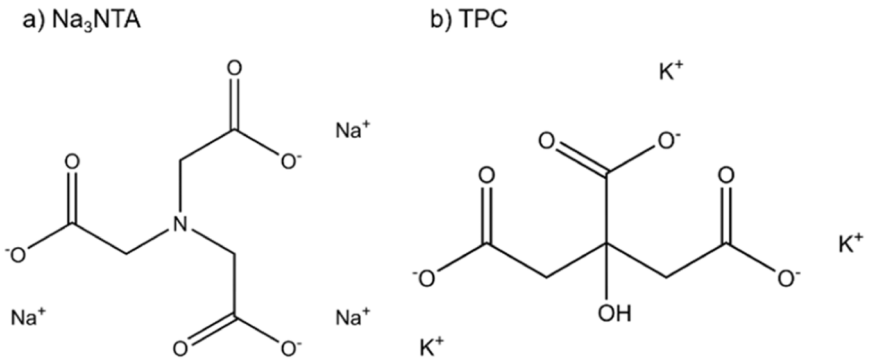

Fig. 2. Chemical structure of a) Na_3NTA and b) TPC.

2.3.2. Structural properties

The compressive strength of the demolded prism samples was measured using a testing bench (Automax 5, Controls) in accordance with EN 196-1 at 7 and 28 d [84]. Each sample underwent six replicate tests, with each prism bar used for two measurements. Due to the insufficient early strength development of the control sample N00 at 1 d, no compressive strength data were obtained for any sample at this age. Following compressive strength testing at 7 and 28 d, and after 1 day of hydration, the fractured sample fragments were further crushed to particles smaller than 4 mm for subsequent analyses. To terminate hydration while preserving the microstructural characteristics, the crushed samples were immersed in isopropanol for 24 h, rinsed with diethyl ether under vacuum filtration, and subsequently dried in a vacuum oven at 40 °C for 8 h.

The microstructural pore properties of hydrated samples at 7 and 28 d were characterized by the MIP porosimeter (AutoPore IV 9500, Micromeritics) with a maximum working pressure of 228 MPa. To mitigate the influence of particle size and the ink-bottle effect [85,86], the previously prepared crushed and dried hydrated samples were further sieved to obtain particles of 1–4 mm. During the measurement, the Hg-solid contact angle was set to 130°, with a mercury surface tension of 485 mN/m.

2.3.3. Mineralogical compositions

The evolution of the phase composition during the hydration process (at 1, 7, and 28 d) was characterized using XRD, TG/DTG, and FTIR. The crushed and dried (hydration-terminated) granular samples (below 4 mm) at each age were further milled into powder using a planetary ball mill (Pulverisette 5, Fritsch) at 240 rpm for 15 min to prepare them for these characterizations.

For the XRD test, the powder was subsequently co-milled with Si (used as an internal standard) in an XRD mill (McCrone, RETSCH) at 3/4 speed for 5 min to facilitate accurate mineral identification and quantification. The XRD analysis was conducted using an X-ray diffractometer (D4 ENDEAVOR, Bruker) with a LynxEye detector. A Co X-ray source, 5–100° 2θ range, 0.014° 2θ step size (1.5 s per step), and 30 rpm stage rotation speed were applied during the process. Following the acquisition of the XRD spectra, the mineral phase identification was performed using DIFFRAC.EVA (Bruker) software. Furthermore, the quantification was conducted using the DIFFRAC.TOPAS (Bruker) software based on Rietveld refinement. Standard crystal structure information files (CIFs) from the Inorganic Crystal Structure Database (ICSD) were utilized as the base of Rietveld refinement, as presented in Table 3.

As hydration progresses, an increasing amount of water is chemically incorporated into the solid phase, leading to an apparent increase in total mineral content when measured after hydration is stopped. This effect can obscure a direct comparison of phase evolution across different hydration stages. To address this issue, the mineral phase content in hydrated samples was normalized (rescaled) to a common reference, the raw (anhydrous) BOF slag state, allowing for a more accurate comparison of phase transformations [87]. It was conducted based on the equation:

$$W_{i,\text{normalized}} = W_{i,\text{Rietveld}} \left(1 - H_2O_{\text{bound}}\right) \quad (1)$$

The 'i' represents every single phase, and the 'H_2O_{bound}' refers to the chemically bonded water determined through subsequent TG/DTG analysis (Fig. 7)

For the TG/DTG analysis, the ball-milled powder was used directly. The measurement was performed using a TG oven (TG 209 F3 Tarsus, NETZSCH) under a nitrogen atmosphere (50 mL/min) to prevent oxidation. The sample was heated from 40 °C to 1000 °C at a heating rate of 10 °C/min. A corundum crucible was employed, and an automated sample carrier (macro-supported) was utilized during the analysis.

The ball-milled powder was also used directly for the FTIR characterization. The analysis was conducted using an MIR/FIR spectrometer (Frontier, PerkinElmer) equipped with an attenuated total reflection (ATR) accessory (GladiATR, Pike). The sample was scanned 20 times at a spectral resolution of 1 cm^{-1} over the wavenumber range 4000–400 cm^{-1}.

2.3.4. Potential environmental impact

To assess the potential environmental impact of the material, particularly in terms of elemental leaching, a one-stage batch leaching test was conducted on raw BOF slag and 28-day hydrated samples. The procedure followed the EN 12457–2 standard [88]. The test materials consisted of (i) crushed hydrated samples without hydration termination, prepared as described in Section 2.3.2, and (ii) sieved raw BOF slag; in both cases, the particle size was below 4 mm. They were mixed with deionized water at a liquid-to-solid ratio of 10 L/kg in the 500 mL PE bottle. The bottles were then placed on an automatic shaker (ES SM-30, Edmund Buhler) and agitated continuously for 24 h to ensure thorough leaching. After shaking, the suspension was left to settle for 30 min, after which the supernatant was collected. The extracted supernatant was filtered by a 0.2 μm syringe filter (Puradisc™ 25). The filtrate was acidified with 1 M concentrated nitric acid to prevent possible precipitation and was then analyzed by ICP-OES (SPECTROBLUE) to quantify the concentrations of leached elements.

Table 3
Crystal structures used in XRD quantification.

Minerals	ICSD code #
Wuestite ($Fe_{0.902}O$)	27237
Magnetite (Fe_3O_4)	26410
Brownmillerite ($Ca_2((Fe_{1.796}Al_{0.204})O_5)$)	98824
Dicalcium Silicate - Alpha' ($Ca_2(SiO_4)$)	81097
Dicalcium Silicate - Beta ($Ca_2(SiO_4)$)	963
Katoite ($Ca_3Al_2(O_4H_4)_3$)	94630
Hydroandradite ($Ca_3Fe_2Si_{1.15}O_{4.6}(OH)_{7.4}$)	29247
Hydrotalcite ($(((Mg_4Al_2)(OH)_{12}(CO_3)(H_2O)_3)_{0.5}$)	6296
Pyroaurite ($((Fe_2Mg_6(OH)_{16}(CO_3)(H_2O)_{4.5})_{0.375}$)	6295
Lime (CaO)	75785
Portlandite ($Ca(OH)_2$)	64950
Calcite ($Ca(CO_3)$)	20179

3. Results and discussion

3.1. Early-age reactions

The heat flow during the initial 48 h and the cumulative heat release over the first 7 days for samples with varying Na_3NTA dosages and an additional ligand-containing sample (C10) are depicted in Fig. 3a and Fig. 3b, respectively. The data have been normalized by the corresponding BOF slag mass. The cumulative heat release was determined by integrating the heat flow after 45 min of sample insertion, thereby removing the interference of the initial (contact) dissolution.

As observed from Fig. 3a, Na_3NTA significantly improves the early hydration rate of BOF slag, as evidenced by the pronounced exothermic peaks in all Na_3NTA-activated samples. In contrast, the signal of the reference specimen N00 converges quickly to the baseline after the initial (contact) dissolution heat flow ends. Among the Na_3NTA-activated samples, N09 demonstrates the highest exothermic peak (around 3.9 mW/g_{slag}) at 1.4 h, followed by two additional peaks at 3.9 and 6.4 h. In the N18 sample, the primary exothermic peak is delayed (4.3 h) and less pronounced (peaking at about 2.8 mW/g_{slag}) compared to N09. A further delay is observed in the N36 sample, where the main exothermic peak occurs at 6.3 h with a lower intensity of 2.3 mW/g_{slag}. The delay and attenuation of the main hydration peaks with increasing Na_3NTA dose may be attributed to the formation of metal-NTA complexes in solution, thus reducing the supersaturation of metal ions that contribute to the matrix formation of hydration products, primarily Ca^{2+}, within the system [89–92]. Besides, the potential adsorption of NTA complexes onto the surfaces of hydration products may delay their

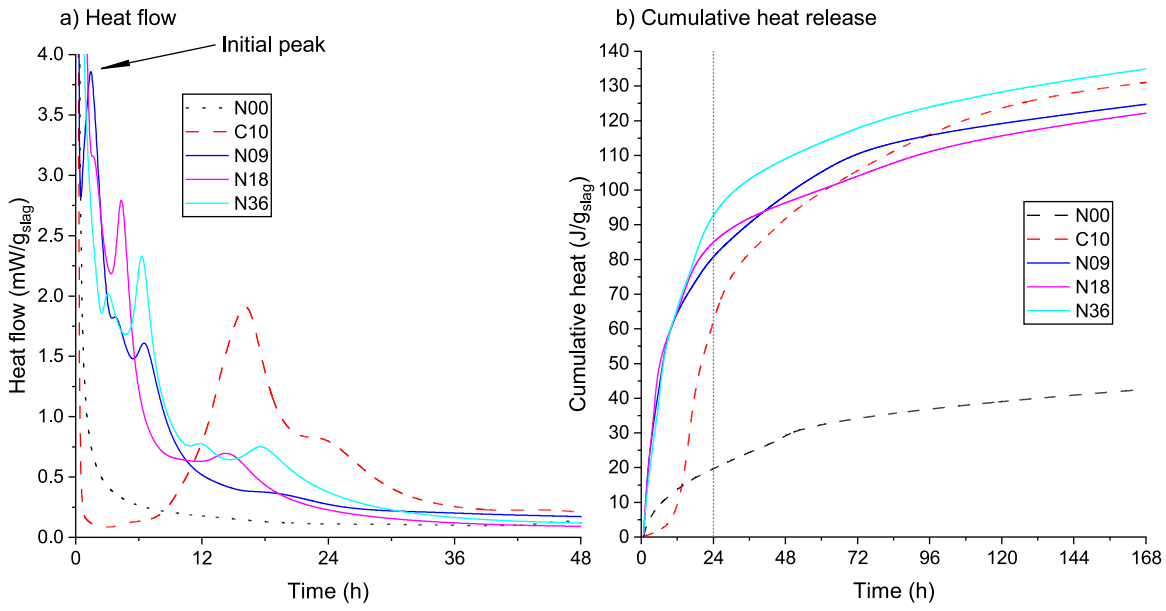

Fig. 3. Hydration heat records of BOF slag pastes a) Heat flow and b) Cumulative heat release.

nucleation and growth [89–93]. Additional exothermic peaks appear in the N18 and N36 curves after 11 h, which are absent in N09. Consequently, as shown in Fig. 3b, the cumulative heat release at 24 h slightly increases with Na_3NTA dosage, indicating a marginally higher early hydration degree. Regardless of the dosage, all Na_3NTA-activated samples exhibit a high early hydration rate, as indicated by the steep slope of the cumulative exotherm curves and the rapid appearance of the heat flow peaks before 12 h. After this initial period, high Na_3NTA dosages continue to markedly enhance BOF slag hydration, resulting in a more pronounced reaction. By 7 days, all Na_3NTA-activated samples exhibit significantly higher cumulative heat release (> 120 J/g_{slag}) than the N00 reference (42 J/g_{slag}), with N36 demonstrating the most pronounced effect.

Comparing the effects of Na_3NTA and TPC, both effectively enhance the reactivity of BOF slag. However, their specific activation patterns, as reflected by the exothermal curves, differ considerably. Sample N09 presents a vigorous hydration heat release peak (as shown in Fig. 3a) shortly after the initial dissolution exotherm and exhibits no induction period commonly observed in traditional Portland cement hydration. In contrast, the TPC-activated sample C10 follows a pattern similar to typical Portland cement hydration, characterized by a distinct induction period following the initial dissolution [87,94]. The very rapid hydration response of Na_3NTA-activated BOF slag, characterized by an essentially immediate onset of reaction without a discernible induction stage, offers both practical potential and a technical imperative to tailor the setting and hardening kinetics to meet the requirements of different engineering applications. The difference of activation patterns between Na_3NTA and TPC is further highlighted in Fig. 3b, where at the very early stages of hydration (before 12 h), N09 exhibits significantly higher cumulative heat release than C10 (64.6 J/g_{slag} at 12 h), despite both being tripodal tetradentate ligands. This difference could be attributed to their distinct chemical structures. The TPC structure contains a hydroxyl (-OH) group, which is absent in Na_3NTA [95]. The presence of -OH in calcium glycolate structures has been shown to form strong hydrogen-bonding networks that adsorb onto the surfaces of reactants and hydration products, thereby exerting a retarding effect [96]. This phenomenon likely accounts for the induction period observed in the hydration of TPC-activated BOF slag. Moreover, the carboxyl group attached to the central carbon atom in TPC is not structurally equivalent to the other two carboxyl groups, unlike in Na_3NTA.

3.2. Evolution of mineral phase compositions

As described in Section 2.3.3, the XRD patterns and corresponding quantitative mineral compositions of hydrated samples at 1, 7, and 28 d, along with the raw BOF slag as a reference, are presented in Fig. 4 and Table 4, respectively. The goodness of fit (GOF) and residual weighted pattern (Rwp) values are also provided in Table 4. Generally, anhydrous raw BOF slag is highly crystalline due to crystallization of the molten slag during slow cooling [97–99]. However, as shown in Table 4, there is an unignorable amount of amorphous phase in the raw BOF slag, which could be attributed to the disruption of the long-range order of crystallites after disc milling and subsequent XRD milling [100].

As shown in Table 4, the main crystalline hydration products of BOF slag are hydrogarnet and hydrotalcite. However, a notable difference exists between the Na_3NTA-activated samples and the reference sample N00 at any age. In the activated samples, hydrogarnet is the principal crystalline hydration product, whereas in N00, hydrotalcite predominates. The hydrogarnet has the general chemical formula $Ca_3(Al_x-Fe_{1-x})_2(SiO_4)_y(OH)_{4(3-y)}$, with a variable ratio of SiO_4^{4-} to $4OH^-$ as well as Al^{3+} to Fe^{3+} [65,101]. The exact formula is difficult to determine, so two end-members, katoite ($Ca_3Al_2(O_4H_4)_3$) and hydroandradite ($Ca_3Fe_2Si_{1.15}O_{4.6}(OH)_{7.4}$), were finally applied in Rietveld refinement. Hydrotalcite shares the same characteristics. It is a brucite-like layered double hydroxide (LDH) with the general formula $Mg_6Al_{2-x}Fe_x(-CO_3)_y(OH)_{(18-2y)}\cdot nH_2O$. Thus, it also possesses variable Al^{3+} to Fe^{3+} and CO_3^{2-} to OH^- ratios. For this reason, hydrotalcite ($Mg_{0.667}Al_{0.333}$)$(OH)_2(CO_3)_{0.167}(H_2O)_{0.5}$) and Fe-bearing pyroaurite ($Mg_6Fe_2(OH)_{16}(OH)(CO_3)(H_2O)_{4.5}$) were included in the Rietveld refinement [102]. Finally, the sum of katoite and hydroandradite is reported as hydrogarnet, and the contribution of hydrotalcite and Fe-bearing pyroaurite is reported as hydrotalcite. As described in Section 2.3.3, the Rietveld refinement QXRD results were corrected (normalized) and are presented in Table 5. The anhydrous phase contents and the resulting calculated hydration degrees are also attached. The magnetite was excluded from the 'anhydrous' due to its negligible reactivity during hydration.

As shown in Table 5, Na_3NTA significantly enhances the consumption of brownmillerite. At an early age (1 d), brownmillerite hydration is markedly promoted by Na_3NTA, decreasing from 14.4 wt% in raw BOF slag to just 5.3 wt% in N36, indicating a significant improvement compared to the control sample N00, where 13.3 wt% of brownmillerite

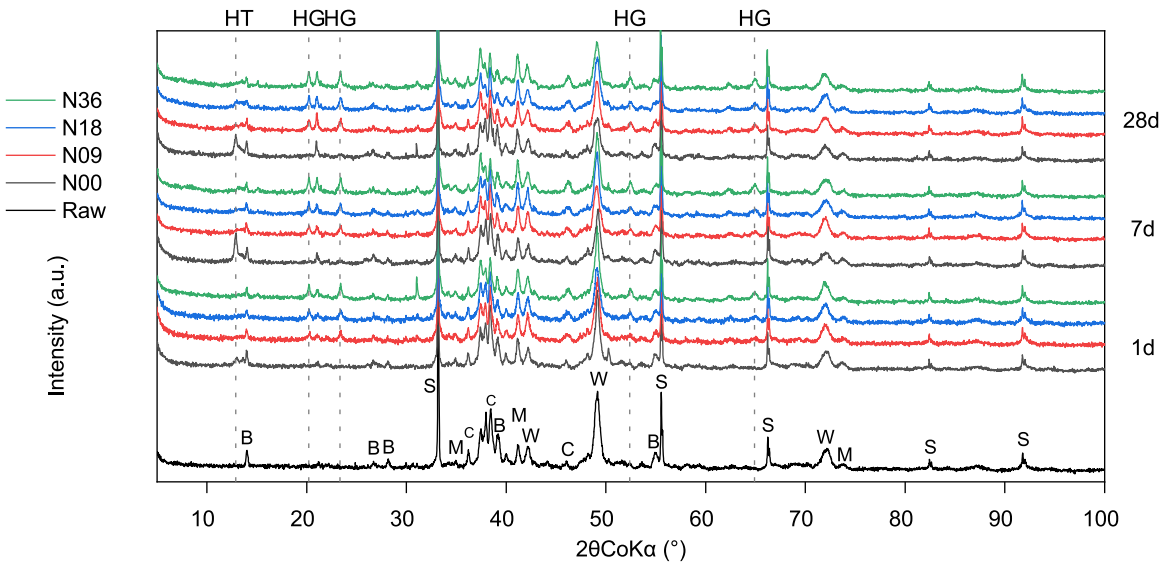

Fig. 4. XRD spectra of hydrated and raw BOF slags (Initial anhydrous phases: B-Brownmillerite, S-Si, M-Magnetite, C-[$C_2S(\alpha' + \beta)$], W-Wuestite; Hydration products: HT-hydrotalcite, HG-Hydrogarnet, P-Portlandite).

Table 4
Quantitative phase compositions of raw and hydrated BOF slags.

Phase	raw BOF	1 d				7 d				28 d			
		N00	N09	N18	N36	N00	N09	N18	N36	N00	N09	N18	N36
Wuestite	25.5	24.7	20.2	19.0	19.5	21.5	20.7	20.7	18.5	19.9	19.1	19.0	18.5
Magnetite	4.4	4.9	4.8	4.8	4.5	4.9	5.9	5.4	4.9	5.6	4.9	5.3	5.2
Brownmillerite	14.4	13.7	7.6	6.9	5.6	14.0	7.3	7.0	6.3	13.9	6.9	6.4	6.5
C_2S (α' + β)	40.3	42.0	36.3	34.0	30.2	40.0	34.0	31.8	25.0	35.5	27.2	27.7	22.0
Hydrogarnet	0.0	1.0	8.5	9.9	14.2	1.2	10.1	11.7	16.4	1.5	11.7	13.7	15.9
Hydrotalcite	0.0	2.9	0.8	1.0	0.9	3.5	1.1	1.8	1.7	4.5	2.0	2.9	2.2
lime	0.9	0.1	0.1	0.0	0.0	0.4	0.0	0.2	0.1	0.3	0.2	0.1	0.0
Portlandite	1.1	0.3	0.1	0.7	1.0	0.4	1.0	1.1	2.1	1.3	1.8	1.6	2.0
Calcite	0.1	0.3	0.8	1.0	1.1	0.0	0.5	0.6	0.9	0.0	0.9	1.0	1.5
Amorphous	13.3	10.2	20.8	22.8	23.0	14.0	19.3	19.8	24.1	17.6	25.2	22.2	26.1
GOF	1.7	1.9	1.7	1.6	1.6	2.0	1.6	1.6	1.6	1.8	1.6	1.6	1.6
Rwp (%)	3.2	3.8	3.1	3.0	2.9	3.8	2.9	2.9	2.9	3.6	2.9	3.0	2.9

Table 5
Phase compositions of raw and normalized hydrated BOF slag.

Phase	Raw BOF	1 d				7 d				28 d			
		N00	N09	N18	N36	N00	N09	N18	N36	N00	N09	N18	N36
Wuestite	25.5	23.9	19.3	18.0	18.4	20.4	19.6	19.5	17.4	18.7	17.8	17.8	17.3
Magnetite	4.4	4.7	4.6	4.6	4.2	4.7	5.6	5.1	4.6	5.3	4.6	5.0	4.9
Brownmillerite	14.4	13.3	7.2	6.5	5.3	13.3	6.9	6.6	5.9	13.0	6.4	6.0	6.1
C_2S (α' + β)	40.3	40.7	34.6	32.3	28.4	37.9	32.2	29.9	23.5	33.4	25.3	26.0	20.6
Hydrogarnet	0.0	1.0	8.1	9.4	13.4	1.1	9.6	11.0	15.4	1.4	10.9	12.9	14.9
Hydrotalcite	0.0	2.8	0.8	0.9	0.9	3.3	1.0	1.7	1.6	4.2	1.9	2.7	2.0
Lime	0.9	0.1	0.1	0.0	0.0	0.4	0.0	0.2	0.1	0.2	0.2	0.1	0.0
Portlandite	1.1	0.3	0.1	0.6	0.9	0.4	1.0	1.0	1.9	1.2	1.7	1.5	1.9
Calcite	0.1	0.2	0.8	1.0	1.0	0.0	0.5	0.5	0.8	0.0	0.8	1.0	1.4
Amorphous	13.3	9.9	19.9	21.6	21.7	13.3	18.3	18.7	22.6	16.5	23.5	20.8	24.4
Anhydrous*	81.1	78.0	61.2	56.8	52.1	72.0	58.8	56.3	46.8	65.4	49.7	50.0	44.0
Hydration degree	0.0	3.9	24.5	29.9	35.8	11.3	27.6	30.6	42.2	19.4	38.8	38.4	45.8

* Sum of: Wuestite, Brownmillerite, C_2S (α' + β), and Lime.

is still left. After 1 d, brownmillerite exhibits minimal additional hydration across all specimens. These results indicate that Na_3NTA, particularly at relatively high dosages, facilitates the near-complete hydration of brownmillerite within the first day. Wuestite follows a similar consumption trend to brownmillerite with the use of Na_3NTA. For example, at 1 d, in N36, it reduces by 7.1 wt% (corresponding to 27.8% of its original content in raw BOF slag) and remains nearly stable at later ages. In contrast, in the control sample N00, wuestite continues to be consumed as age increases, reaching levels similar to those in the activated samples at 28 d. This phenomenon suggests that, beyond the initial rapid dissolution facilitated by Na_3NTA, wuestite itself has a moderate hydration capacity, likely driven by a gradual increase in pore solution pH over time [103]. The magnetite content remains essentially stable throughout the entire period in all samples.

As shown in Table 5, Na_3NTA also significantly promotes the (early) hydration of C_2S. At 1 d, the C_2S hydration degree substantially increases with increasing Na_3NTA dosage, from 14.1% in N09 to 29.5% in N36. However, brownmillerite is significantly more reactive in the presence of Na_3NTA. Even in N09, brownmillerite depletes by 7.2 wt%, 50.0% of its original content, substantially higher than the 29.5% consumption of C_2S in N36. This phenomenon suggests that Na_3NTA exhibits distinct phase-specific hydration-promoting effects, with a preference for the Fe-rich brownmillerite over the primarily Ca-bearing C_2S. Such differential promotion is likely governed by the varying chelation affinities of NTA^{3-} toward different metal ions [104,105], as indicated by the distinct stability constants in Table 6. Notably, the stability constant of Fe-NTA is several orders of magnitude higher than that of Ca-NTA. Between 1 and 7d C_2S continues to react and decreases by 4.9 wt% in N36. In the other samples, C_2S decreases only from 2.4 wt % to 2.8 wt%. At 28 d, around 50% of the C_2S has reacted in the N36 sample, while it is only around 35% in the other two Na_3NTA-activated specimens. The hydration behavior of C_2S between 7 and 28 d differs notably from that observed from 1 to 7 d. During the early stage (1–7 d), the greatest C_2S consumption occurs in the N36 specimen, reaching 4.9 wt%. In contrast, from 7 to 28 d, the N09 sample shows the highest C_2S consumption (6.9 wt%), substantially exceeding that of N18 (3.9 wt %) and N36 (2.9 wt%). This shift suggests that the strong promoting effect of high-dose Na_3NTA on C_2S hydration is primarily evident at early ages but diminishes at relatively later stages. On the contrary, with a relatively low Na_3NTA dosage (N09), C_2S appears to contribute significantly more to hydration at relatively late ages [58,60,61,106]. The reaction degrees of brownmillerite and C_2S with 0.9 wt% Na_3NTA (this study, Tables 4) and 1.0 wt% TPC (Rietveld QXRD results in [40]) activation (equivalent molar doses, ≈ 32.7 mmol kg^{-1} BOF slag), at 7 and 28 d are compared in Fig. 5. Na_3NTA produces a markedly stronger early-age activation of brownmillerite than TPC after 7 days of hydration; between 7 and 28 d brownmillerite contents remain essentially unchanged with both activators. For C_2S, Na_3NTA also yields greater reaction at 7 d relative to TPC, but between 7 and 28 d, the change in C_2S hydration is larger for the TPC-activated specimen (although its absolute C_2S reaction remains slightly lower than that with Na_3NTA). These results indicate distinct activation regimes for Na_3NTA and TPC: Na_3NTA produces a faster, stronger early activation (a larger reaction of brownmillerite and C_2S up to 7 d). These contrasting behaviours could be ascribed to differences in chemical structure(discussed in Section 3.1) and to the apparently stronger chelation capacity of Na_3NTA, as reflected by its higher stability constants listed in Table 6 [105,107–109].

At all investigated ages, the amorphous fraction generally increases with the Na_3NTA dosage. The increase closely mirrors the progression of C_2S hydration. For instance, from 7 to 28 d, the N09 specimen exhibits the largest increase in amorphous content (5.2 wt%), which aligns with its largest C_2S consumption (6.9 wt%).

Concerning crystalline hydration products, significantly greater amounts of hydrogarnet form in Na_3NTA-activated samples than in the reference at all ages, with its content increasing proportionally to the Na_3NTA dosage. The majority of the hydrogarnet forms during the first day of hydration, which correlates with the consumption of brownmillerite, suggesting that hydrogarnet primarily forms from the hydration of brownmillerite. Silica-free Fe-katoite (C-F-H) is a metastable end-member of the hydrogarnet mineral group that is typically present only in trace amounts under ambient conditions, plausibly because Fe $(OH)_3$ precipitates are thermodynamically favored [65,101,110].

Table 6
(Standard) stability constant (Log Ksp) of NTA^{3-} and $citrate^{3-}$ with common metals in BOF slag [105,107–109].

Ligand (ions)	Ca^{2+}	Fe^{3+}	Mg^{2+}	Al^{3+}
$Citrate^{3-}$	3.5	11.2	3.5	8.0
NTA^{3-}	6.4	15.9	5.5	11.4

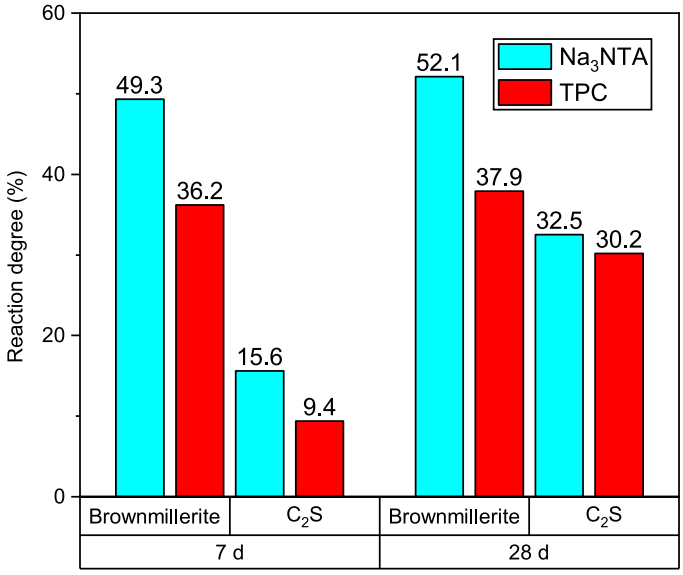

Fig. 5. Reaction degrees of brownmillerite and C_2S under 0.9 wt% of Na_3NTA and 1.0 wt% of TPC (same molar concentration relative to BOF slag) activation.

Hence, the hydroandradite (C-F-S-H) should be the stable form of Fe-bearing hydrogarnet, which means it contains some Si supplied by the hydration of C_2S. Hydrotalcite shows the opposite trend to hydrogarnet. At all three investigated ages, it is more abundant in the reference sample (N00) than in the Na_3NTA-activated samples. Wuestite is the principal likely Mg source for hydrotalcite. However, more wuestite reacts in the Na_3NTA-activated samples than in the reference at 1 d. This apparent discrepancy may be attributed to the intercalation of NTA (complexes) into the interlayer space of hydrotalcite. This intercalation can reduce crystallinity, thereby reducing the detectable hydrotalcite via XRD despite enhanced Mg-bearing precursor (wuestite) dissolution.

To further investigate the hydration products, the TG and derived DTG curves at 1, 7, and 28 d were recorded and are shown in Fig. 6. The results indicate that, at all ages, Na_3NTA-activated samples exhibit greater total weight loss than the reference sample N00, particularly at early ages. Moreover, the extent of weight loss increases with increasing Na_3NTA concentration.

Fig. 6a presents the TG and DTG curves at 1 d. The weight loss below 200 °C is commonly attributed to the dehydration of C-S-H [87]. However, the increase in this range with higher Na_3NTA dosage is modest (from 1.9 wt% in N00 and N09 to 2.3 wt% in N36) and does not fully correspond to the normalized QXRD results in Table 5, which indicate more pronounced amorphous phase formation in the activated samples. Since hydrotalcite is also a major hydration product in this system, its interlayer water and hydroxyl groups are likely to contribute significantly to this weight loss [102,111]. Therefore, the weight loss below 200 °C is attributed to the combined dehydration of C–S–H and hydrotalcite. The 200–400 °C region primarily corresponds to the dehydroxylation of both hydrogarnet and hydrotalcite [65,102,111–113]. The associated weight loss increases from 1.1 wt% in N00 to 3.1 wt% in N36, which is consistent with the increasing sum of hydrogarnet and hydrotalcite contents (Table 5). The weight loss observed between 400 and 500 °C primarily corresponds to the dehydroxylation of portlandite (CH) [87,114]. It is low across all samples. The weight loss between 600 and 800 °C is typically attributed to the decarbonation of calcite [87,114]. This loss increases with the Na_3NTA dosages (from 0.2 wt% in N00 and N09 vs. 1.1 wt% in N36). The DTG peak around 700 °C in N00 shifts to slightly lower temperatures in N09, while in N18 and N36, an additional peak appears starting at approximately 500 °C. Weight loss between 500 and 600 °C can be attributed to the decarbonation of hydrotalcite interlayer carbonates [95,102,115]. However, this weight loss increases

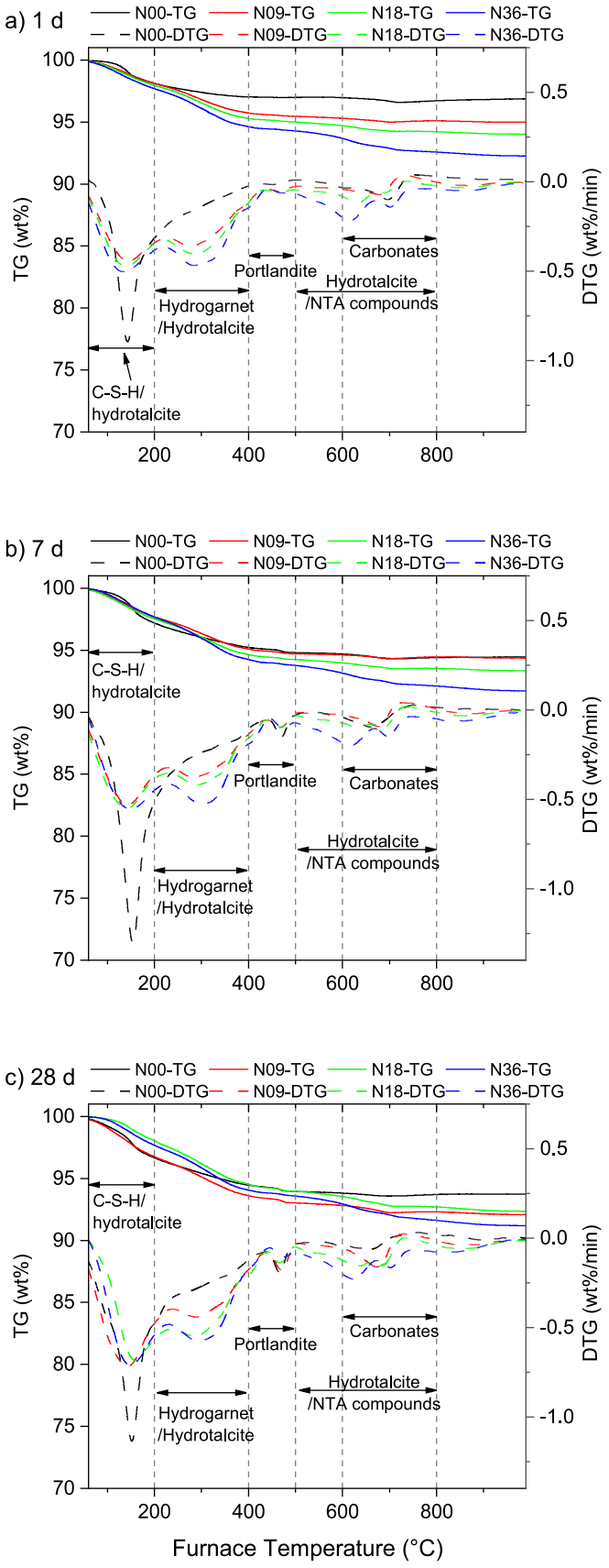

Fig. 6. TG/DTG curves of BOF slag samples at 1, 7, and 28 d.

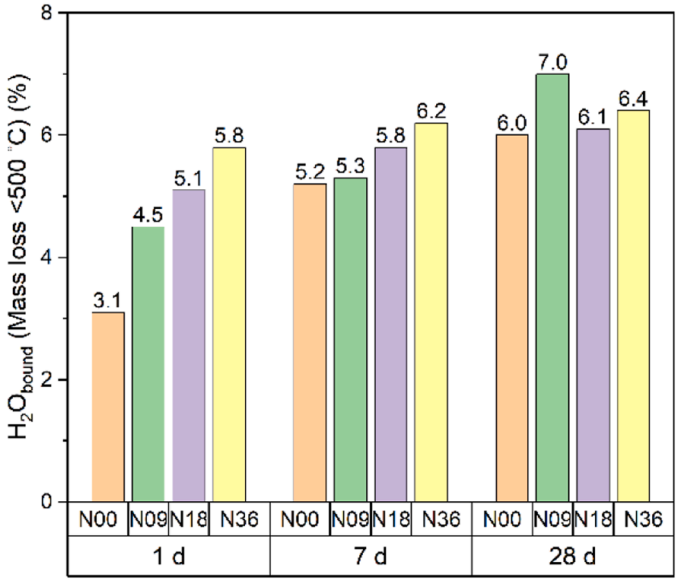

Fig. 7. Content of H_2O_{bound} within hydrated samples (%, mass loss below 500 °C in TG).

with the Na_3NTA dosage (from 0 in N00 to 0.6 wt% in N36) in this study, despite the lower hydrotalcite contents. This anomaly may suggest that the decarboxylation of the (possibly) retained NTA compounds, which increases with the Na_3NTA dosage, may also contribute to this weight loss. Given these observations, the weight loss within 500–800 °C is classified as the decarbonation or decarboxylation of both 'hydrotalcite/NTA compounds' (500–600 °C) and 'carbonates' (600–800 °C). Overall, the results indicate that Na_3NTA promotes the formation of the hydrogarnet and NTA-related compounds during early hydration at 1 d. The weight loss of hydrated samples within the < 200, 200–400, 400–500, and 500–800 °C temperature ranges is presented in Table 7, based on the above discussion and the inferred phases corresponding to the weight loss in each temperature range.

The TG/DTG analysis at 7 d is shown in Fig. 6b. The weight loss below 200 °C shows a slight departure from the 1-day pattern, with the largest mass loss observed in the reference sample N00 (2.8 wt%). The weight loss between 200 and 400 °C follows a similar trend to that at 1 d, increasing from 2.0 wt% in N00 to 3.4 wt% in N36, consistent with the greater hydrogarnet/hydrotalcite content in Na_3NTA-activated specimens. The weight loss ascribed to portlandite (CH) dehydroxylation (400–500 °C) is similar across all samples, ranging from 0.4 wt% to 0.5 wt%. The weight loss in the 500–800 °C range increases with Na_3NTA dosage (0.3 wt% in N09 to 1.6 wt% in N36). This trend is consistent with the 1-day result and suggests that the retention of NTA-related compounds may persist during ongoing hydration. The TG/DTG

Table 7
Mass loss within different temperature ranges of hydrated samples.

Temperature	Age	N00 loss	N09 loss	N18 loss	N36 loss
(°C)	(d)	(%)	(%)	(%)	(%)
< 200	1	1.9	1.9	2.1	2.3
< 200	7	2.8	2.3	2.5	2.3
< 200	28	3.3	3.2	2.0	2.3
200–400	1	1.1	2.4	2.7	3.1
200–400	7	2.0	2.6	2.9	3.4
200–400	28	2.2	3.2	3.5	3.6
400–500	1	0.1	0.2	0.3	0.4
400–500	7	0.4	0.4	0.4	0.5
400–500	28	0.5	0.6	0.6	0.5
500–800	1	0.2	0.4	0.8	1.7
500–800	7	0.4	0.3	0.7	1.6
500–800	28	0.2	0.7	1.2	1.9

profiles at 28 d (Fig. 6c) exhibit thermal-decomposition features broadly consistent with those observed at 7 d. Across all temperature intervals, the mass-loss behaviour follows comparable patterns.

Collectively, these TG/DTG results corroborate the XRD-characterized phase evolution, indicating enhanced formation of hydrogarnet and NTA-related compounds under Na_3NTA activation.

As discussed in the TG analysis, the NTA-related compounds may remain within the hydrated matrix, which was investigated and is discussed below based on the FTIR test. As presented in Fig. 8, the absorption peak at 1598 cm^{-1} in Na_3NTA-activated samples corresponds to the stretching vibration of the carboxylic group ($R\text{-}COO^-$), indicating the presence of NTA compounds [116,117]. At 1 d, the $R\text{-}COO^-$ signal and a pronounced intensity difference could be observed among the three Na_3NTA-activated samples, with higher Na_3NTA doses correlating with stronger signals. This Na_3NTA dose-dependent $R\text{-}COO^-$ signal intensity difference suggests that increased carboxylate content is present in the solid fraction with higher Na_3NTA doses. Given our rigorous solvent-exchange procedure to halt hydration, it is believed that a fraction of NTA (complexes) is strongly retained by early hydration products during the first day of hydration. One potential host phase for NTA (complexes) is hydrotalcite, given its interlayer space that can accommodate anions. As discussed for the XRD analysis, the intercalation of NTA complexes into interlayers also reduces the crystallinity of hydrotalcite.

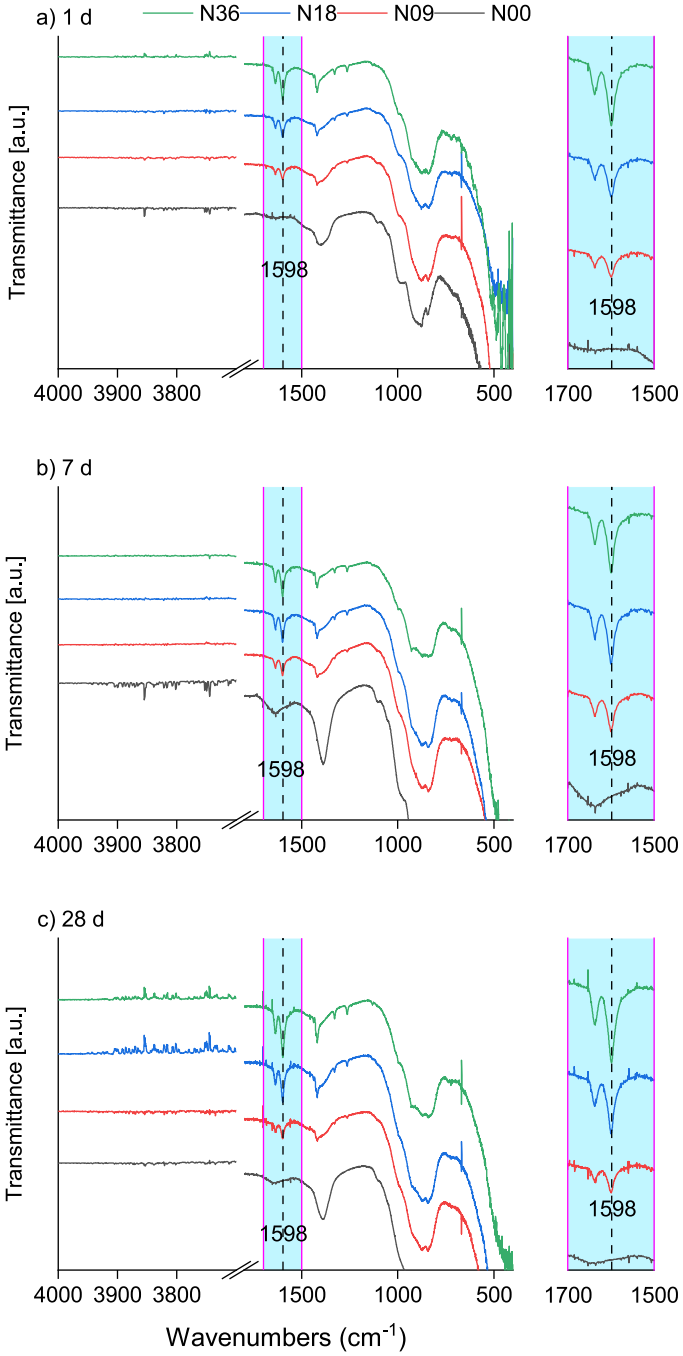

Fig. 8. FTIR spectra of hydrated BOF slag pastes at 1, 7, and 28 d.

3.3. Mechanical strength and pore properties

The compressive strengths of all samples at 7 and 28 d are presented in Fig. 9. As observed, Na_3NTA-activated specimens exhibit significantly higher compressive strength than the reference (N00) at both ages. At 7 d, the strengths of activated samples are nearly an order of magnitude greater than that of N00, and strength increases systematically with Na_3NTA dosage. From 7 to 28 d, the compressive strength of N00 approximately triples; nevertheless, its 28-day strength remains substantially lower than that of the Na_3NTA-activated specimens. At 28 d, the N36 sample attains the highest strength (35.0 MPa), while the strength differences among the three activated mixtures are smaller than those observed at 7 d. These results indicate that Na_3NTA substantially accelerates early-age strength development and that, in general, higher dosages produce greater mechanical gains. Considering the evolution of hydraulically reactive phases from 7 to 28 d, as shown in Table 5, the strength gain between 7 and 28 d should be primarily attributable to continued C_2S hydration in both the reference and activated samples.

Pore properties of all hydrated samples, including porosity, mean pore size, and pore size volume distribution, were characterized through the MIP test and are presented in Fig. 10. As shown in Fig. 10a, at 7 d, Na_3NTA-activated samples exhibit substantially lower porosity than the reference (N00); porosity declines progressively with increasing Na_3NTA dosage (34.6% in N00 to 20.2% in N36). The mean pore size follows the same downward trend. After 28 days of hydration, the pores of all samples are further refined. The effects of Na_3NTA dosage generally remain consistent with that observed at 7 d: higher Na_3NTA concentrations lead to lower porosity and reduced mean pore sizes. In addition to porosity and average pore radius, the influence of Na_3NTA on the relative pore size (volume) distribution of each specimen is illustrated in Fig. 10b. The pores are classified as macropore (>100 nm), capillary pore (10–100 nm), and gel pore (<10 nm) here [118–121]. At 7 d, Na_3NTA dramatically reduces the macropore volume fraction from 77% in N00 to 22% in N36, with concomitant increases in capillary and

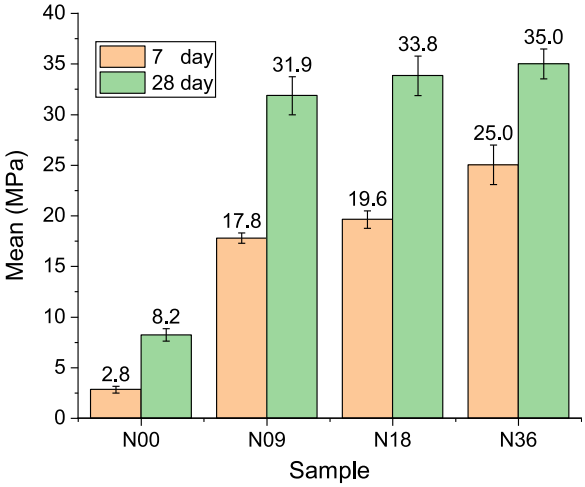

Fig. 9. Compressive strength of NTA-activated BOF slag paste.

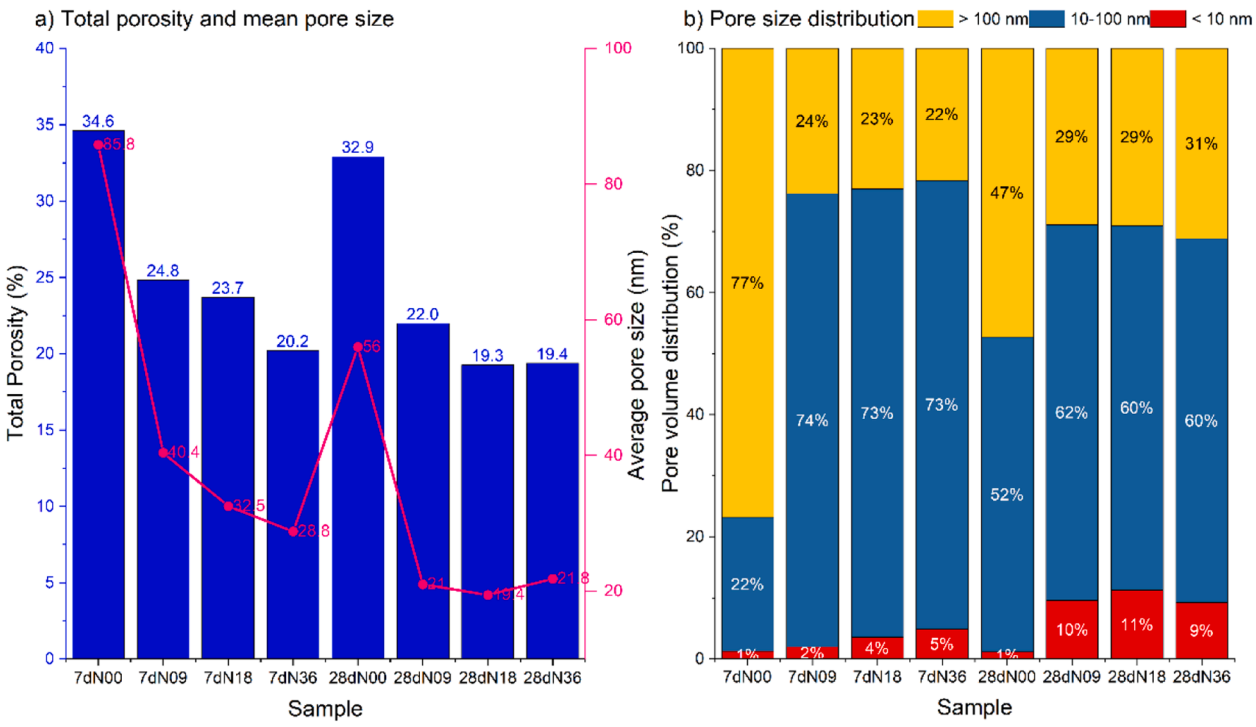

Fig. 10. Pore characteristics of hydrated samples at 7 and 28 d.

gel pore fractions from 22% and 1% (N00) to 73% and 5% (N36), respectively. A similar trend is observed at 28 d, with Na_3NTA-activated samples exhibiting lower macropore percentages and substantially higher gel pore percentages compared to N00. The pore size distribution of N00 also becomes more refined over time: its macropore volume fraction decreases, and the capillary pore fraction increases, consistent with its compressive strength development, which, as discussed previously, should be primarily attributed to the hydration of C_2S.

To comprehensively elucidate the effect of Na_3NTA on BOF slag hydration degree and its related effects on porosity and compressive strength, a Pearson correlation analysis was conducted based on the QXRD-derived hydration degree (Table 5), porosity (Fig. 10), and compressive strength (Fig. 9) of 7 and 28-day hydrated samples. The results are presented in Table 8.

The results show a very strong negative correlation between hydration degree and porosity ($r = -0.962$, $p < 0.001$), a very strong negative correlation between porosity and compressive strength ($r = -0.948$, $p < 0.001$), and a very strong positive correlation between hydration degree and compressive strength ($r = 0.951$, $p < 0.001$). The correlation relationships indicate that: 1) the advancement of hydration effectively reduces pore volume through the formation and accumulation of hydrates, 2) porosity is the primary factor governing the mechanical performance of the hydrated BOF slag system, and 3) the enhancement in mechanical performance is closely associated with the progression of hydration reactions and the formation of load-bearing hydrates. These observations are consistent with the well-established hydration degree-porosity-strength relationship in cementitious materials [122–125]. Overall, these findings indicate a clear mechanistic pathway in Na_3NTA-activated BOF slag: the enhancement in hydration degree promotes the formation of C–S–H gel and hydrogarnet, which progressively fill and refine the pores. This densification improves load-bearing capacity, thereby increasing compressive strength.

Table 8
Pearson correlation analysis of porosity, compressive strength, and hydration degree of 7 and 28-day samples.

		Porosity	Compressive strength	Hydration degree
Porosity	Correlation coefficient	1.00000	-0.94797*	-0.96175*
	p-value		0.00034	0.00014
Compressive strength	Correlation coefficient	-0.94797*	1.00000	0.95088*
	p-value	0.00034		0.00029
Hydration degree	Correlation coefficient	-0.96175*	0.95088*	1.00000
	p-value	0.00014	0.00029	

* : Correlation is significant at the 0.05 (p-value) level.

3.4. Leaching potential

As discussed in the introduction, leaching remains a critical concern when using BOF slag as a building material due to its considerable amount of potentially hazardous heavy metals, particularly vanadium (V) and chromium (Cr) [2,4,40,126]. To evaluate the effect of Na_3NTA on BOF slag leaching behavior, a one-stage batch leaching test was conducted on all hydrated samples at 28 d and on the raw BOF slag. The concentrations of leached Cr and V, the legal thresholds specified by the Dutch Soil Quality Code (DSQC), and the pH of the leachates are presented in Table 9 [127].

In BOF slag, Cr primarily exists in the brownmillerite phase in its trivalent form, substituting Fe in the octahedral coordination site (B-site), and is partially incorporated into the spinel-type RO solid solution phase [4,126,128,129]. Due to its stable trivalent state and octahedral coordination, Cr generally exhibits low mobility and toxicity [126,128]. In contrast, V primarily resides in C_2S, replacing Si in the tetrahedral coordination site in its tetravalent or pentavalent states—both toxic [129–132]. Additionally, V exists in brownmillerite in its trivalent form, occupying an octahedral coordination site [126,128,133]. Trivalent vanadium (V(III) is prone to oxidation, converting to its pentavalent form (V(V)), the most toxic and mobile state, accompanied by a shift in coordination symmetry from octahedral to tetrahedral [126,128,132]. Consequently, V generally exhibits a higher leaching tendency than Cr, frequently appearing in its highly mobile and toxic pentavalent state [126,128,129]. Furthermore, V is present in significantly higher

Table 9
Legal thresholds of the DSQC and tested heavy metal leaching values (pH values of leachates attached).

Element	DSQC threshold (mg/kg)	Raw BOF slag (mg/kg)	N00 (mg/kg)	N09 (mg/kg)	N18 (mg/kg)	N36 (mg/kg)
Cr	0.63	0.24	0.01	0.01	0.02	0.03
V	1.8	3.66	0.02	0.16	0.12	0.25
pH	/	12.2	12.7	12.8	12.7	12.8

Below detection threshold (BDT): Ag, As, Be, Bi, Cd, Co, Cu, Ga, In, Ni, Hg, Pb, Sb, Se, Sn

concentrations than Cr in the original BOF slag, as illustrated in Table 1. This higher concentration, coupled with its greater mobility and toxicity, underscores its environmental risk and necessitates vigilant monitoring and management.

As shown in Table 9, Cr release from unhydrated BOF slag is measurable but remains below regulatory limits, whereas V release from the raw material markedly exceeds the DSQC threshold. In contrast, leachate concentrations of both Cr and V from 28-day hydrated samples, both Na_3NTA-activated and the reference (N00), are substantially reduced and lie well below legal thresholds, indicating effective immobilization during hydration. This immobilization is likely facilitated by Fe or Al octahedral coordination sites within hydrogarnet, SiO_4^{2-} tetrahedral coordination sites in C-S-H, and the interlayer regions of hydrotalcite [45,134–138].

Considering the effects of Na_3NTA, the leaching of both Cr and V generally increases with Na_3NTA dosage. This trend can be attributed to the chelation of NTA^{3-} with Cr and V, leading to the formation of soluble (and thus leachable) NTA-metal complexes [54,74,139,140]. Although the hydration products in BOF slag contribute to immobilizing these metals, resulting in significantly lower Cr and V leaching than raw BOF slag, the presence of Na_3NTA enhances their release relative to the reference sample N00. Moreover, V leaching is more affected by Na_3NTA than Cr, which may be partially explained by the higher chelation affinity of NTA^{3-} for V (III, IV, and V) compared to Cr(III), as indicated by the greater stability constants of V-NTA complexes relative to Cr (III)-NTA [107,108,141]. Additionally, under highly alkaline conditions (pH > 12), V, particularly in its V(IV) and V(V) oxidation states, exhibits higher solubility than Cr(III) which tends to hydrolyze and precipitate as insoluble hydroxides [142–144]. This greater solubility makes V more susceptible to chelation by NTA^{3-} in alkaline environments. Another possible explanation for this disparity in leaching behavior is the distinct phase distribution of Cr and V within BOF slag. A substantial fraction of Cr is sequestered within the RO phase, limiting its availability for chelation by Na_3NTA. In contrast, V is predominantly hosted within C_2S, where it substitutes for Si in active tetrahedral coordination sites, making it more accessible for complexation and subsequent leaching.

4. Conclusion

This study presents the first investigation of Na_3NTA as a hydration activator for BOF slag. Four doses of Na_3NTA, including a zero dose as the reference, were applied during the research, and their effects on BOF slag hydration were comprehensively investigated. The following key conclusions can be drawn:

1) Na_3NTA significantly accelerates the early hydration of BOF slag, as evidenced by pronounced exothermic peaks and substantially increased cumulative heat release in isothermal calorimetry. Unlike TPC-activated BOF slag, which exhibits a distinct induction period, Na_3NTA-activated samples demonstrate an immediate and vigorous hydration reaction without an induction phase, highlighting fundamental differences in their activation patterns.
2) The inherent reactivity of the reference BOF slag is very limited; only small amounts of C_2S and wuestite are consumed over time, and the main reaction products are hydrotalcite and C-S-H gel. Whereas Na_3NTA significantly promotes the hydration of the primary potentially reactive phases, brownmillerite and C_2S, leading to the formation of crystalline hydrogarnet and C-S-H gel. At high Na_3NTA dosages, brownmillerite hydration is nearly complete within one day, accompanied by significantly enhanced C_2S hydration. Furthermore, FTIR spectroscopy indicates that NTA (complexes) are rapidly incorporated into the hydrated matrix soon after the onset of hydration.
3) The activation of Na_3NTA leads to a denser microstructure of BOF slag paste, as evidenced by reduced porosity and a finer pore size distribution, as measured by MIP. These microstructural improvements correlate with substantial enhancements in mechanical performance, with Na_3NTA-activated samples exhibiting significantly higher compressive strengths than the reference sample at both 7 and 28 d. Compressive strength and microstructure improvement generally increase with the Na_3NTA dosage at each age.
4) Hydrated BOF slag immobilizes Cr and V well within the solid matrix, resulting in significantly lower leaching than raw BOF slag, with concentrations well below legal limits. Even so, Na_3NTA does facilitate the leaching of Cr and V, with V leaching being more substantially affected than Cr.

CRediT authorship contribution statement

Zhihan Jiang: Writing – original draft, Validation, Methodology, Investigation, Formal analysis, Data curation, Conceptualization. **Helong Song:** Writing – review & editing, Funding acquisition, Formal analysis. **Xuan Ling:** Writing – review & editing, Investigation, Formal analysis. **Tao Liu:** Writing – review & editing, Formal analysis. **Katrin Schollbach:** Writing – review & editing, Supervision, Funding acquisition. **H.J.H Brouwers:** Writing – review & editing, Supervision, Formal analysis.

Declaration of Competing Interest

The authors declare that they have no known competing financial interests or personal relationships that could have appeared to influence the work reported in this paper.

Acknowledgment

This research was supported by the China Scholarship Council (fund No. 202006950032), National Natural Science Foundation of China (Grant No. 52500171), Guangdong Basic and Applied Basic Research Foundation (No. 2026A1515012027), 868/The Third Phase of High-Level University Construction (fund No. 000001033378). The authors sincerely appreciate the assistance of Anneke Delsing with the ICP-OES test and Peter Lipman with the MIP test. We also thank Tata Steel (The Netherlands) for providing the raw BOF slag used in this study.

Data availability

Data will be made available on request.

References

[1] I.Z. Yildirim, M. Prezzi, Chemical, mineralogical, and morphological properties of steel slag, Adv. Civ. Eng. 2011 (2011) 463638, https://doi.org/10.1155/2011/463638.
[2] Y. Jiang, T.C. Ling, C. Shi, S.Y. Pan, Characteristics of steel slags and their use in cement and concrete-a review, Resour. Conserv. Recycl 136 (2018) 187–197, https://doi.org/10.1016/j.resconrec.2018.04.023.
[3] Q. Wang, P. Yan, Hydration properties of basic oxygen furnace steel slag, Constr. Build. Mater. 24 (2010) 1134–1140, https://doi.org/10.1016/j.conbuildmat.2009.12.028.

[4] W.F. Santos, K. Schollbach, S. Melzer, S.R. van der Laan, H.J.H. Brouwers, Quantitative analysis and phase assemblage of basic oxygen furnace slag hydration, J. Hazard. Mater. 450 (2023) 131029, https://doi.org/10.1016/j.jhazmat.2023.131029.
[5] E. Belhadj, C. Diliberto, A. Lecomte, Characterization and activation of Basic Oxygen Furnace slag, Cem. Concr. Compos 34 (2012) 34–40, https://doi.org/10.1016/j.cemconcomp.2011.08.012.
[6] 2023 World Steel Statistics, 2023. ⟨https://worldsteel.org/data/world-steel-in-figures/world-steel-in-figures-2024/⟩.
[7] T.C. Alex, G. Mucsi, T. Venugopalan, S. Kumar, BOF steel slag: critical assessment and integrated approach for utilization, J. Sustain. Met. 7 (2021) 1407–1424, https://doi.org/10.1007/S40831-021-00435-2/FIGURES/8.
[8] İ. Yüksel, A Review of Steel Slag Usage in Construction Industry for Sustainable Development, Springer Netherlands, 2017, https://doi.org/10.1007/s10668-016-9759-x.
[9] C. van Hoek, J. Small, S. van der Laan, Large-area phase mapping using phase recognition and characterization (PARC) software, Micros. Today 24 (2016) 12–21, https://doi.org/10.1017/S1551929516000572.
[10] S.K. Singh, P. Rekha, M. Surya, Utilization of Linz–Donawitz slag from steel industry for waste minimization, J. Mater. Cycles Waste Manag 22 (2020) 611–627, https://doi.org/10.1007/s10163-020-00981-z.
[11] A.C.P. Martins, J.M. Franco de Carvalho, L.C.B. Costa, H.D. Andrade, T.V. de Melo, J.C.L. Ribeiro, L.G. Pedroti, R.A.F. Peixoto, Steel slags in cement-based composites: an ultimate review on characterization, applications and performance (undefined-undefined), Constr. Build. Mater. 291 (2021), https://doi.org/10.1016/j.conbuildmat.2021.123265.
[12] Q. Dong, G. Wang, X. Chen, J. Tan, X. Gu, Recycling of steel slag aggregate in portland cement concrete: an overview, J. Clean. Prod. 282 (2021) 124447, https://doi.org/10.1016/j.jclepro.2020.124447.
[13] Y. Xue, S. Wu, H. Hou, J. Zha, Experimental investigation of basic oxygen furnace slag used as aggregate in asphalt mixture, J. Hazard. Mater. 138 (2006) 261–268, https://doi.org/10.1016/J.JHAZMAT.2006.02.073.
[14] Z. Chen, J. Xie, Y. Xiao, J. Chen, S. Wu, Characteristics of bonding behavior between basic oxygen furnace slag and asphalt binder, Constr. Build. Mater. 64 (2014) 60–66, https://doi.org/10.1016/j.conbuildmat.2014.04.074.
[15] Q. Wang, D. Wang, S. Zhuang, The soundness of steel slag with different free CaO and MgO contents, Constr. Build. Mater. 151 (2017) 138–146, https://doi.org/10.1016/j.conbuildmat.2017.06.077.
[16] G. Wang, Y. Wang, Z. Gao, Use of steel slag as a granular material: volume expansion prediction and usability criteria, J. Hazard. Mater. 184 (2010) 555–560, https://doi.org/10.1016/j.jhazmat.2010.08.071.
[17] Euroslag STATISTICS 2021, (n.d.) ⟨https://www.euroslag.com/products/statistics/stati⟩.
[18] H. Na, Y.J. Wang, X. Zhang, J.G. Li, Y.N. Zeng, P.Y. Liu, Hydration activity and carbonation characteristics of dicalcium silicate in steel slag: a review, Metals 11 (2021) 1580, https://doi.org/10.3390/met11101580.
[19] W. Qiang, S. Mengxiao, Y. Jun, Influence of classified steel slag with particle sizes smaller than 20 μm on the properties of cement and concrete, Constr. Build. Mater. 123 (2016) 601–610, https://doi.org/10.1016/j.conbuildmat.2016.07.042.
[20] S.K. Singh, P.Vashistha Jyoti, Development of newer composite cement through mechano-chemical activation of steel slag, Constr. Build. Mater. 268 (2021) 121147, https://doi.org/10.1016/j.conbuildmat.2020.121147.
[21] Q. Wang, J. Yang, P. Yan, Cementitious properties of super-fine steel slag, Powder Technol. 245 (2013) 35–39, https://doi.org/10.1016/j.powtec.2013.04.016.
[22] S. Liu, L. Li, Influence of fineness on the cementitious properties of steel slag, J. Therm. Anal. Calor. 117 (2014) 629–634, https://doi.org/10.1007/S10973-014-3789-0/FIGURES/10.
[23] J.C.O. Zepper, S.R. van der Laan, K. Schollbach, H.J.H. Brouwers, Reactivity of BOF slag under autoclaving conditions, Constr. Build. Mater. 364 (2023) 129957, https://doi.org/10.1016/j.conbuildmat.2022.129957.
[24] A. Duda, Hydraulic reactions of LD steelwork slags, Cem. Concr. Res. 19 (1989) 793–801, https://doi.org/10.1016/0008-8846(89)90050-1.
[25] Y. Tang, K. Schollbach, S. van der Laan, W. Chen, Activation of BOF slag with dipotassium hydrogen phosphate: enhancing hydration, carbonation resistance, and heavy metal leaching, Cem. Concr. Compos. 157 (2025) 105922, https://doi.org/10.1016/j.cemconcomp.2025.105922.
[26] M. Zhu, Q. Yu, S.R. van der Laan, Y. Chen, Dipotassium hydrogen phosphate activated Al-rich steel slag: the role of layered double hydroxides and aluminum hydrate gel, Cem. Concr. Res. 189 (2025) 107783, https://doi.org/10.1016/j.cemconres.2025.107783.
[27] J. Sun, Z. Chen, Effect of silicate modulus of water glass on the hydration of alkali-activated converter steel slag, J. Therm. Anal. Calor. 138 (2019) 47–56, https://doi.org/10.1007/s10973-019-08146-3.
[28] M. Zhu, Y. Chen, S.R. van der Laan, T. Liu, Q. Yu, Sodium aluminate activated BOF steel slag: impact of Al(OH)4− on reaction mechanism, Cem. Concr. Res. 201 (2026) 108116, https://doi.org/10.1016/j.cemconres.2025.108116.
[29] Y. Tang, K. Schollbach, Z. Liu, S. van der Laan, W. Chen, H.J.H. Brouwers, Phosphate-activated basic oxygen furnace (BOF) slag: understanding pH-driven hydration and strength development, Cem. Concr. Res. 199 (2026) 108034, https://doi.org/10.1016/j.cemconres.2025.108034.
[30] J. Li, W. Ni, X. Wang, S. Zhu, X. Wei, F. Jiang, H. Zeng, M. Hitch, Mechanical activation of medium basicity steel slag under dry condition for carbonation curing, J. Build. Eng. 50 (2022) 104123, https://doi.org/10.1016/J.JOBE.2022.104123.
[31] S. Yadav, A. Mehra, Experimental study of dissolution of minerals and CO2 sequestration in steel slag, Waste Manag 64 (2017) 348–357, https://doi.org/10.1016/J.WASMAN.2017.03.032.
[32] Q. Song, M.Z. Guo, L. Wang, T.C. Ling, Use of steel slag as sustainable construction materials: a review of accelerated carbonation treatment, Resour. Conserv. Recycl 173 (2021), https://doi.org/10.1016/j.resconrec.2021.105740.
[33] G. Biava, M. Zajac, A. Principallo, L.E. Depero, M. Ben Haha, E. Bontempi, Evaluation of steel slags in CO2 sequestration and as supplementary cementitious material, Constr. Build. Mater. 489 (2025) 142271, https://doi.org/10.1016/J.CONBUILDMAT.2025.142271.
[34] G. Liu, K. Schollbach, P. Li, H.J.H. Brouwers, Valorization of converter steel slag into eco-friendly ultra-high performance concrete by ambient CO2 pre-treatment, Constr. Build. Mater. 280 (2021) 122580, https://doi.org/10.1016/J.CONBUILDMAT.2021.122580.
[35] L. Mo, F. Zhang, M. Deng, F. Jin, A. Al-Tabbaa, A. Wang, Accelerated carbonation and performance of concrete made with steel slag as binding materials and aggregates, Cem. Concr. Compos 83 (2017) 138–145, https://doi.org/10.1016/j.cemconcomp.2017.07.018.
[36] M. Zajac, I. Maruyama, A. Iizuka, J. Skibsted, Enforced carbonation of cementitious materials, Cem. Concr. Res. 174 (2023) 107285, https://doi.org/10.1016/J.CEMCONRES.2023.107285.
[37] L. Chang, H. Liu, J. Wang, L. Song, Y. Wang, S. Cui, Effect of chelation via ethanol-diisopropanolamine on hydration of pure steel slag, Constr. Build. Mater. 357 (2022) 129372, https://doi.org/10.1016/j.conbuildmat.2022.129372.
[38] J. Wang, L. Chang, D. Yue, Y. Zhou, H. Liu, Y. Wang, S. Yang, S. Cui, Effect of chelating solubilization via different alkanolamines on the dissolution properties of steel slag, J. Clean. Prod. 365 (2022) 132824, https://doi.org/10.1016/j.jclepro.2022.132824.
[39] S. Yvars, K. Schollbach, T. Wattez, S. Van der Laan, H.J.H. Brouwers, Influence of limestone filler on potassium citrate activated BOF slag binder, Constr. Build. Mater. 494 (2025) 143424, https://doi.org/10.1016/J.CONBUILDMAT.2025.143424.
[40] A.M. Kaja, K. Schollbach, S. Melzer, S.R. van der Laan, H.J.H. Brouwers, Q. Yu, Hydration of potassium citrate-activated BOF slag, Cem. Concr. Res. 140 (2021) 106291, https://doi.org/10.1016/j.cemconres.2020.106291.
[41] W. Franco Santos, J.J. Botterweg, S. Chaves Figueiredo, K. Schollbach, S. van der Laan, H.J.H. Brouwers, Sodium oxalate activation of basic oxygen furnace slag for building materials, Resour. Conserv. Recycl 198 (2023) 107174, https://doi.org/10.1016/j.resconrec.2023.107174.
[42] K. Gu, Y. Maierdan, B. Chen, Effects of ethylenediamine tetra-acetic acid (EDTA) and its disodium salt derivative (EDTA-Na) on the characteristics of magnesium oxysulfate (MOS) cement, Compos. Part B Eng. 232 (2022) 109654, https://doi.org/10.1016/J.COMPOSITESB.2022.109654.
[43] L. Chi, W. Li, Z. Li, Z. Wang, S. Lu, Q. Liu, Investigation of the hydration properties of cement with EDTA by alternative current impedance spectroscopy, Cem. Concr. Compos. 126 (2022) 104365, https://doi.org/10.1016/j.cemconcomp.2021.104365.
[44] J. Wang, Y. Wang, H. Liu, L. Chang, H. Wang, Y. Wang, S. Cui, Effect of disodium EDTA on hydration and mechanical properties of calcium sulphoaluminate-belite cement, Cem. Concr. Res. 164 (2023) 107041, https://doi.org/10.1016/J.CEMCONRES.2022.107041.
[45] R.E. Guidone, X. Gaona, F. Winnefeld, M. Altmaier, H. Geckeis, B. Lothenbach, Citrate sorption on cement hydrates, Cem. Concr. Res. 178 (2024) 107404, https://doi.org/10.1016/J.CEMCONRES.2023.107404.
[46] Z. Jiang, X. Ling, Q. Liu, H. Song, K. Schollbach, H.J.H. Brouwers, Basic oxygen furnace (BOF) slag cementitious binder activated by Na4EDTA, Cem. Concr. Res. 198 (2025) 107983, https://doi.org/10.1016/j.cemconres.2025.107983.
[47] Z. Jiang, J. Zepper, X. Ling, K. Schollbach, H.J.H. Brouwers, Potassium citrate-activated pure BOF slag-based mortars utilizing carbonated and autoclaved BOF slag aggregates, Cem. Concr. Compos 150 (2024) 105564, https://doi.org/10.1016/j.cemconcomp.2024.105564.
[48] Y. Zhang, M. Zhou, A critical review of the application of chelating agents to enable Fenton and Fenton-like reactions at high pH values, J. Hazard. Mater. 362 (2019) 436–450, https://doi.org/10.1016/J.JHAZMAT.2018.09.035.
[49] R. Paris, K.V. Desboeufs, Effect of atmospheric organic complexation on iron-bearing dust solubility, Atmos. Chem. Phys. 13 (2013) 4895–4905, https://doi.org/10.5194/ACP-13-4895-2013.
[50] Z. Wang, W.D.C. Schenkeveld, S.M. Kraemer, D.E. Giammar, Synergistic effect of reductive and ligand-promoted dissolution of goethite, Environ. Sci. Technol. 49 (2015) 7236–7244, https://doi.org/10.1021/acs.est.5b01191.
[51] E.M. Saad, X. Wang, N.J. Planavsky, C.T. Reinhard, Y. Tang, Redox-independent chromium isotope fractionation induced by ligand-promoted dissolution, Nat. Commun. 8 (2017) 1–10, https://doi.org/10.1038/s41467-017-01694-y.
[52] Z. Zhang, M.W. Bligh, X. Yuan, T.D. Waite, Ligand-promoted reductive cleaning of iron-fouled membranes from submerged membrane bioreactors, J. Memb. Sci. 545 (2018) 126–132, https://doi.org/10.1016/j.memsci.2017.09.059.
[53] A.E. Martell, R.J. Motekaitis, A.R. Fried, J.S. Wilson, D.T. MacMillan, Thermal decomposition of EDTA, NTA, and nitrilotrimethylenephosphonic acid in aqueous solution, Can. J. Chem. 53 (1975) 3471–3476, https://doi.org/10.1139/v75-498.
[54] I.S.S. Pinto, I.F.F. Neto, H.M.V.M. Soares, Biodegradable chelating agents for industrial, domestic, and agricultural applications—a review, Environ. Sci. Pollut. Res. 21 (2014) 11893–11906, https://doi.org/10.1007/s11356-014-2592-6.
[55] Y.V. Nancharaiah, N. Schwarzenbeck, T.V.K. Mohan, S.V. Narasimhan, P. A. Wilderer, V.P. Venugopalan, Biodegradation of nitrilotriacetic acid (NTA) and ferric–NTA complex by aerobic microbial granules, Water Res 40 (2006) 1539–1546, https://doi.org/10.1016/J.WATRES.2006.02.006.

[56] R.J. Larson, R.M. Ventullo, Kinetics of biodegradation of nitrilotriacetic acid (NTA) in an estuarine environment, Ecotoxicol. Environ. Saf. 12 (1986) 166–179, https://doi.org/10.1016/0147-6513(86)90054-0.
[57] F. Yin, J. Li, Y. Wang, Z. Yang, Biodegradable chelating agents for enhancing phytoremediation: mechanisms, market feasibility, and future studies, Ecotoxicol. Environ. Saf. 272 (2024) 116113, https://doi.org/10.1016/J.ECOENV.2024.116113.
[58] M. Zajac, J. Skocek, B. Lothenbach, B.H. Mohsen, Late hydration kinetics: indications from thermodynamic analysis of pore solution data, Cem. Concr. Res. 129 (2020) 105975, https://doi.org/10.1016/J.CEMCONRES.2020.105975.
[59] R. Trettin, G. Oliew, C. Stadelmann, W. Wieker, Very early hydration of dicalcium silicate-polymorphs, Cem. Concr. Res. 21 (1991) 757–764, https://doi.org/10.1016/0008-8846(91)90171-D.
[60] H. El-Didamony, A.M. Sharara, I.M. Helmy, S.Abd El-Aleem, Hydration characteristics of β-C2S in the presence of some accelerators, Cem. Concr. Res. 26 (1996) 1179–1187, https://doi.org/10.1016/0008-8846(96)00103-2.
[61] A.J.M. Cuberos, Á.G. De la Torre, M.C. Martín-Sedeño, L. Moreno-Real, M. Merlini, L.M. Ordónez, M.A.G. Aranda, Phase development in conventional and active belite cement pastes by Rietveld analysis and chemical constraints, Cem. Concr. Res. 39 (2009) 833–842, https://doi.org/10.1016/J.CEMCONRES.2009.06.017.
[62] Y. Luo, S.H. Li, K.M. Klima, H.J.H. Brouwers, Q. Yu, Degradation mechanism of hybrid fly ash/slag based geopolymers exposed to elevated temperatures, Cem. Concr. Res. 151 (2022) 106649, https://doi.org/10.1016/j.cemconres.2021.106649.
[63] Y.M. Kim, S.H. Hong, Influence of minor ions on the stability and hydration rates of β-dicalcium silicate, J. Am. Ceram. Soc. 87 (2004) 900–905, https://doi.org/10.1111/j.1551-2916.2004.00900.x.
[64] B.Z. Dilnesa, E. Wieland, B. Lothenbach, R. Dähn, K.L. Scrivener, Fe-containing phases in hydrated cements, Cem. Concr. Res. 58 (2014) 45–55, https://doi.org/10.1016/j.cemconres.2013.12.012.
[65] B.Z. Dilnesa, B. Lothenbach, G. Renaudin, A. Wichser, D. Kulik, Synthesis and characterization of hydrogarnet Ca3(AlxFe1 − x)2(SiO4)y(OH)4(3 − y), Cem. Concr. Res. 59 (2014) 96–111, https://doi.org/10.1016/J.CEMCONRES.2014.02.001.
[66] K.L. Scrivener, T. Füllmann, E. Gallucci, G. Walenta, E. Bermejo, Quantitative study of Portland cement hydration by X-ray diffraction/Rietveld analysis and independent methods, Cem. Concr. Res. 34 (2004) 1541–1547, https://doi.org/10.1016/J.CEMCONRES.2004.04.014.
[67] M. Diaferio, F.B. Varona Moya, L. Lavagna, R. Nisticò, An insight into the chemistry of cement—a review, Vol. 13, Page 203, Appl. Sci. 2023 13 (2022) 203, https://doi.org/10.3390/APP13010203.
[68] E. John, B. Lothenbach, Cement hydration mechanisms through time – a review, J. Mater. Sci. 58 (2023) 9805–9833, https://doi.org/10.1007/S10853-023-08651-9/FIGURES/4.
[69] E. Gartner, D. Myers, Influence of tertiary alkanolamines on portland cement hydration, J. Am. Ceram. Soc. 76 (1993) 1521–1530, https://doi.org/10.1111/j.1151-2916.1993.tb03934.x.
[70] Z. Lu, X. Kong, D. Jansen, C. Zhang, J. Wang, X. Pang, J. Yin, Towards a further understanding of cement hydration in the presence of triethanolamine, Cem. Concr. Res. 132 (2020) 106041, https://doi.org/10.1016/j.cemconres.2020.106041.
[71] X. Huang, F. Wang, S. Hu, Y. Lu, M. Rao, Y. Mu, Brownmillerite hydration in the presence of gypsum: the effect of Al/Fe ratio and sulfate ions, J. Am. Ceram. Soc. 102 (2019) 5545–5554, https://doi.org/10.1111/JACE.16384.
[72] A. Mériot, S. Gauffinet, M.N. de Noirfontaine, M. Courtial, K. Alloncle, L. Izoret, F. Dunstetter, Hydration in diluted solutions of brownmillerite extracted from SR cement and synthetic brownmillerite, Cem. Concr. Res. 181 (2024) 107518, https://doi.org/10.1016/J.CEMCONRES.2024.107518.
[73] W. Schwarz, Novel cement matrices by accelerated hydration of the ferrite phase in portland cement via chemical activation: kinetics and cementitious properties, Adv. Cem. Based Mater. 2 (1995) 189–200, https://doi.org/10.1016/1065-7355(95)90003-9.
[74] A. Polettini, R. Pomi, E. Rolle, D. Ceremigna, L. De Propris, M. Gabellini, A. Tornato, A kinetic study of chelant-assisted remediation of contaminated dredged sediment, J. Hazard. Mater. 137 (2006) 1458–1465, https://doi.org/10.1016/j.jhazmat.2006.04.022.
[75] A. Eivazihollagh, I. Svanedal, H. Edlund, M. Norgren, On chelating surfactants: molecular perspectives and application prospects, J. Mol. Liq. 278 (2019) 688–705, https://doi.org/10.1016/j.molliq.2019.01.076.
[76] B. Nowack, J.M. VanBriesen, Chelating agents in the environment 12 (2005) 1–18, https://doi.org/10.1021/BK-2005-0910.CH001.
[77] I.V. T.D. Perry, O.W. Duckworth, T.A. Kendall, S.T. Martin, R. Mitchell, Chelating ligand alters the microscopic mechanism of mineral dissolution, J. Am. Chem. Soc. 127 (2005) 5744–5745, https://doi.org/10.1021/ja042737k.
[78] N. Carrasco, R. Kretzschmar, M.L. Pesch, S.M. Kraemer, Effects of anionic surfactants on ligand-promoted dissolution of iron and aluminum hydroxides, J. Colloid Interface Sci. 321 (2008) 279–287, https://doi.org/10.1016/j.jcis.2008.02.011.
[79] Z. Wang, H. Fu, L. Zhang, W. Song, J. Chen, Ligand-promoted photoreductive dissolution of goethite by atmospheric low-molecular dicarboxylates, J. Phys. Chem. A. 121 (2017) 1647–1656, https://doi.org/10.1021/acs.jpca.6b09160.
[80] M. Biver, W. Shotyk, Experimental study of the kinetics of ligand-promoted dissolution of stibnite (Sb 2S 3), Chem. Geol. 294–295 (2012) 165–172, https://doi.org/10.1016/j.chemgeo.2011.11.009.
[81] Nitrilotriacetic Acid Trisodium Salt ChemWatch Review SDS, 2022.
[82] J.R. Hart, Ullmann's Encyclopedia of Industrial Chemistry, Wiley-VCH, Weinheim, 2000, https://doi.org/10.1002/14356007.a10_095.
[83] NITRILOTRIACETIC ACID TRISODIUM SALT, 2003. ⟨https://www.ilo.org/dyn/icsc/showcard.display?p_version=2&p_card_id=1240⟩.
[84] British Standards Institution., Methods of testing cement. Part 1, Determination of strength., (n.d.) 33. ⟨https://www.en-standard.eu/bs-en-196-1-2016-methods-of-testing-cement-determination-of-strength/⟩ (accessed July 25, 2023).
[85] N. Hearn, R.D. Hooton, Sample mass and dimension effects on mercury intrusion porosimetry results, Cem. Concr. Res. 22 (1992) 970–980, https://doi.org/10.1016/0008-8846(92)90121-B.
[86] F. Moro, H. Böhni, Ink-Bottle effect in mercury intrusion porosimetry of cement-based materials, J. Colloid Interface Sci. 246 (2002) 135–149, https://doi.org/10.1006/JCIS.2001.7962.
[87] K. Scrivener, R. Snellings, B. Lothenbach, A practical guide to microstructural analysis of cementitious materials, CRC Press, 2016, https://doi.org/10.1201/B19074.
[88] European Committee for Standardizaiton, EN 12457-2, Characterisation of Waste. Leaching. Compliance Test for Leaching of Granular Waste Materials and Sludges, 2014.
[89] J. Prywer, E. Mielniczek-Brzóska, M. Olszynski, Struvite crystal growth inhibition by trisodium citrate and the formation of chemical complexes in growth solution, J. Cryst. Growth 418 (2015) 92–101, https://doi.org/10.1016/j.jcrysgro.2015.02.027.
[90] A. Viani, L. Zárybnická, R. Ševčík, P. Mácová, J. Machotová, K. Veltruská, Struvite-K crystal growth inhibition by citric acid: formation of complexes in solution and surface adsorption effects, J. Cryst. Growth 598 (2022) 126858, https://doi.org/10.1016/j.jcrysgro.2022.126858.
[91] A. Viani, L. Zárybnická, R. Ševčík, P. Mácová, J. Machotová, Mechanisms of controlled crystallization of struvite-K by NTA and EDTA sodium salts, J. Cryst. Growth 623 (2023) 127414, https://doi.org/10.1016/J.JCRYSGRO.2023.127414.
[92] F. Jones, A. Oliveira, A.L. Rohl, M.I. Ogden, G.M. Parkinson, Understanding the mechanism by which nitrilotriacetic acid interacts with precipitating barium sulfate, CrystEngComm 8 (2006) 869–876, https://doi.org/10.1039/B608302A.
[93] S.P. Gopi, K. Palanisamy, V.K. Subramanian, Effect of NTA and temperature on crystal growth and phase transformations of CaCO3, Desalin. Water Treat. 54 (2015) 316–324, https://doi.org/10.1080/19443994.2014.883332.
[94] W. Kurdowski, Cement and Concrete Chemistry, Springer Netherlands, Dordrecht, 2014, https://doi.org/10.1007/978-94-007-7945-7.
[95] R. Ramaswamy, M. Illikainen, J. Yliniemi, Influence of ligands as chemical admixtures in the early hydration of sodium carbonate-activated blast furnace slag, Constr. Build. Mater. 422 (2024) 135753, https://doi.org/10.1016/j.conbuildmat.2024.135753.
[96] O. Chaudhari, J.J. Biernacki, S. Northrup, Effect of carboxylic and hydroxycarboxylic acids on cement hydration: experimental and molecular modeling study, J. Mater. Sci. 52 (2017) 13719–13735, https://doi.org/10.1007/s10853-017-1464-0.
[97] C. Thomas, J. Rosales, J.A. Polanco, F. Agrela, Steel slags, N. Trends Eco-Effic. Recycl. Concr. (2019) 169–190, https://doi.org/10.1016/B978-0-08-102480-5.00007-5.
[98] C.W. Bale, P. Chartrand, S.A. Degterov, G. Eriksson, K. Hack, R. Ben Mahfoud, J. Melançon, A.D. Pelton, S. Petersen, Crystallization behavior of BOF slag during the cooling process towards leaching for CO2 sequestration, Process Saf. Environ. Prot. 191 (2024) 2663–2673, https://doi.org/10.1016/S0364-5916(02)00035-4.
[99] M. woo Choi, S.M. Jung, Crystallization behavior of melted BOF slag during non-isothermal constant cooling process, J. Non Cryst. Solids 468 (2017) 105–112, https://doi.org/10.1016/j.jnoncrysol.2017.04.042.
[100] A.W. Weeber, H. Bakker, Amorphization by ball milling. A review, Phys. B Condens. Matter 153 (1988) 93–135, https://doi.org/10.1016/0921-4526(88)90038-5.
[101] C.A. Geiger, G.R. Rossman, Micro- And nano-size hydrogarnet clusters and proton ordering in calcium silicate garnet: Part I- And quest to understand the nature of "water" in garnet continues, Am. Miner. 105 (2020) 455–467, https://doi.org/10.2138/am-2020-7256.
[102] K. Rozov, U. Berner, C. Taviot-Gueho, F. Leroux, G. Renaudin, D. Kulik, L. W. Diamond, Synthesis and characterization of the LDH hydrotalcite–pyroaurite solid-solution series, Cem. Concr. Res. 40 (2010) 1248–1254, https://doi.org/10.1016/J.CEMCONRES.2009.08.031.
[103] I. Strandkvist, Å. Sandström, F. Engström, Effect of FeO/MgO ratio on dissolution and leaching of magnesiowüstite, Steel Res. Int. 88 (2017) 1600322, https://doi.org/10.1002/SRIN.201600322.
[104] Chelation chemistry, (n.d.). ⟨www.dow.com/documents/113/113-01388-01-chelation-chemistry-general-concepts-of-the-chemistry-of-chelation.pdf?iframe=true&⟩.
[105] R.M. Smith, A.E. Martell, Critical stability constants, enthalpies and entropies for the formation of metal complexes of aminopolycarboxylic acids and carboxylic acids, Sci. Total Environ. 64 (1987) 125–147, https://doi.org/10.1016/0048-9697(87)90127-6.
[106] A. Cuesta, A. Ayuela, M.A.G. Aranda, Belite cements and their activation, Cem. Concr. Res. 140 (2021) 106319, https://doi.org/10.1016/j.cemconres.2020.106319.
[107] R.M. Smith, A.E. Martell, Second Supplement, 1976. https://doi.org/10.1007/978-1-4757-5506-0.
[108] G. ANDEREGG, Critical evaluation of equilibrium constants in solution part a: stability constants of metal complexes critical survey of stability constants of NTA

complexes, UNION PURE Appl. Chem. 54 (1982) 2693–2758, https://doi.org/10.1351/PAC198254122693/MACHINEREADABLECITATION/RIS.
[109] A.E. Martell, R.M. Smith, First Supplement, 1982. https://doi.org/10.1007/978-1-4615-6761-5.
[110] D.E. Rogers, L.P. Aldridge, Hydrates of calcium ferrites and calcium aluminoferrites, Cem. Concr. Res. 7 (1977) 399–409, https://doi.org/10.1016/0008-8846(77)90068-0.
[111] E. Kanezaki, Thermal behavior of the hydrotalcite-like layered structure of Mg and Al-layered double hydroxides with interlayer carbonate by means of in situ powder HTXRD and DTA/TG, Solid State Ion. 106 (1998) 279–284, https://doi.org/10.1016/S0167-2738(97)00494-3.
[112] M. Zajac, S.K. Bremseth, M. Whitehead, M. Ben Haha, Effect of CaMg(CO3)2 on hydrate assemblages and mechanical properties of hydrated cement pastes at 40 °C and 60 °C, Cem. Concr. Res. 65 (2014) 21–29, https://doi.org/10.1016/J.CEMCONRES.2014.07.002.
[113] Chloride-binding capacity of Hydrotalcite in Cement Pastes Containing Dolomite and Metakaolin, Cem. Concr. Res. 107 (2018) 163–181. https://doi.org/10.1016/J.CEMCONRES.2018.02.002.
[114] A. Morandeau, M. Thiéry, P. Dangla, Investigation of the carbonation mechanism of CH and C-S-H in terms of kinetics, microstructure changes and moisture properties, Cem. Concr. Res. 56 (2014) 153–170, https://doi.org/10.1016/j.cemconres.2013.11.015.
[115] S.J. Palmer, H.J. Spratt, R.L. Frost, Thermal decomposition of hydrotalcites with variable cationic ratios, J. Therm. Anal. Calorim. 95 (2009) 123–129, https://doi.org/10.1007/S10973-008-8992-4/METRICS.
[116] Y. Tomita, T. Ando, K. Ueno, Infrared spectra of nitrilotriacetate chelates in aqueous solution, J. Phys. Chem. 69 (1965) 404–407, https://doi.org/10.1021/j100886a008.
[117] S. Tang, Y. Deng, S.Z. Zhan, Chloro-free route to mixed-metal oxides. Synthesis of lead titanate nanoparticles from a single-source precursor route, J. Therm. Anal. Calorim. 104 (2011) 653–659, https://doi.org/10.1007/S10973-010-0999-Y/FIGURES/8.
[118] N. Li, C. Shi, Z. Zhang, Understanding the roles of activators towards setting and hardening control of alkali-activated slag cement, Compos. Part B Eng. 171 (2019) 34–45, https://doi.org/10.1016/j.compositesb.2019.04.024.
[119] Q. Zeng, K. Li, T. Fen-Chong, P. Dangla, Pore structure characterization of cement pastes blended with high-volume fly-ash, Cem. Concr. Res. 42 (2012) 194–204, https://doi.org/10.1016/J.CEMCONRES.2011.09.012.
[120] Y. Gu, R.P. Martin, O. Omikrine Metalssi, T. Fen-Chong, P. Dangla, Pore size analyses of cement paste exposed to external sulfate attack and delayed ettringite formation, Cem. Concr. Res. 123 (2019) 105766, https://doi.org/10.1016/J.CEMCONRES.2019.05.011.
[121] R. Kumar, B. Bhattacharjee, Porosity, pore size distribution and in situ strength of concrete, Cem. Concr. Res. 33 (2003) 155–164, https://doi.org/10.1016/S0008-8846(02)00942-0.
[122] I. Odler, M. Rößler, Investigations on the relationship between porosity, structure and strength of hydrated Portland cement pastes. II. Effect of pore structure and of degree of hydration, Cem. Concr. Res. 15 (1985) 401–410, https://doi.org/10.1016/0008-8846(85)90113-9.
[123] X. Chen, S. Wu, J. Zhou, Influence of porosity on compressive and tensile strength of cement mortar, Constr. Build. Mater. 40 (2013) 869–874, https://doi.org/10.1016/J.CONBUILDMAT.2012.11.072.
[124] H. Ahmadi Moghadam, A. Mirzaei, Z. Abedi Dehghi, The relation between porosity, hydration degree and compressive strength of Portland cement pastes in the presence of aluminum chloride additive, Constr. Build. Mater. 250 (2020) 118884, https://doi.org/10.1016/j.conbuildmat.2020.118884.
[125] H. Song, F. Gauvin, T. Liu, X. Sun, Z. Dong, F. Wang, X. Chen, H.J.H. Brouwers, Understanding of municipal solid waste incineration (MSWI) bottom ash/cement blends: impact of natural fiber on mechanical strength and leaching behavior, J. Build. Eng. 120 (2026) 115330, https://doi.org/10.1016/j.jobe.2026.115330.
[126] P. Chaurand, J. Rose, J. Domas, J.Y. Bottero, Speciation of Cr and V within BOF steel slag reused in road constructions, J. Geochem. Explor 88 (2006) 10–14, https://doi.org/10.1016/j.gexplo.2005.08.006.
[127] Soil Quality Decree, 2015. ⟨https://wetten.overheid.nl/BWBR0023085/2015-07-01#BijlageA⟩.
[128] P. Chaurand, J. Rose, O. Proux, J.L. Hazemann, V. Briois, M. Salome, J. Susini, J. H. Ferrasse, D. Borschneck, J.Y. Bottero, Environmental impact of steel slag reused as aggregates in road manufacturing: molecular mechanisms of chromium and vanadium release, AIP Conf. Proc. 882 (2007) 199–201, https://doi.org/10.1063/1.2644473.
[129] L. De Windt, P. Chaurand, J. Rose, Kinetics of steel slag leaching: batch tests and modeling, Waste Manag. 31 (2011) 225–235, https://doi.org/10.1016/J.WASMAN.2010.05.018.
[130] M.J. Ahmed, R. Cuijpers, K. Schollbach, S. Van Der Laan, M. Van Wijngaarden-Kroft, T. Verhoeven, H.J.H. Brouwers, V and Cr substitution in dicalcium silicate under oxidizing and reducing conditions – synthesis, reactivity, and leaching behavior studies, J. Hazard. Mater. 442 (2023) 130032, https://doi.org/10.1016/j.jhazmat.2022.130032.
[131] H. Preßlinger, K.O. Klepp, Vanadium in converter slags, Steel Res. 73 (2002) 522–525, https://doi.org/10.1002/srin.200200022.
[132] P. Chaurand, J. Rose, V. Briois, M. Salome, O. Proux, V. Nassif, L. Olivi, J. Susini, J.L. Hazemann, J.Y. Bottero, New methodological approach for the vanadium K-edge X-ray absorption near-edge structure interpretation: application to the speciation of vanadium in oxide phases from steel slag, J. Phys. Chem. B 111 (2007) 5101–5110, https://doi.org/10.1021/jp063186i.
[133] S. Wunderlich, T. Schirmer, U.E.A. Fittschen, Investigation on vanadium chemistry in basic-oxygen-furnace (BOF) slags—a first approach, Metals 11 (2021) 1869, https://doi.org/10.3390/met11111869.
[134] A. Vollpracht, W. Brameshuber, Binding and leaching of trace elements in Portland cement pastes, Cem. Concr. Res. 79 (2016) 76–92, https://doi.org/10.1016/J.CEMCONRES.2015.08.002.
[135] M.L.D. Gougar, B.E. Scheetz, D.M. Roy, Ettringite and C-S-H portland cement phases for waste ion immobilization: a review, Waste Manag 16 (1996) 295–303, https://doi.org/10.1016/S0956-053X(96)00072-4.
[136] S. Hillier, D.G. Lumsdon, R. Brydson, E. Paterson, Hydrogarnet: a host phase for Cr(VI) in chromite ore processing residue (COPR) and other high pH wastes, Environ. Sci. Technol. 41 (2007) 1921–1927, https://doi.org/10.1021/ES0621997/SUPPL_FILE/ES0621997SI20061220_075011.PDF.
[137] B. Ma, A. Fernandez-Martinez, S. Grangeon, C. Tournassat, N. Findling, F. Claret, A. Koishi, N.C.M. Marty, D. Tisserand, S. Bureau, E. Salas-Colera, E. Elkaïm, C. Marini, L. Charlet, Evidence of multiple sorption modes in layered double hydroxides using Mo As structural probe, Environ. Sci. Technol. 51 (2017) 5531–5540, https://doi.org/10.1021/ACS.EST.7B00946/ASSET/IMAGES/LARGE/ES-2017-00946D_0005.JPEG.
[138] A. Kindness, A. Macias, F.P. Glasser, Immobilization of chromium in cement matrices, Waste Manag 14 (1994) 3–11, https://doi.org/10.1016/0956-053X(94)90016-7.
[139] M. Soleimani, M.A. Hajabbasi, M. Afyuni, S. Akbar, J.K. Jensen, P.E. Holm, O. K. Borggaard, Comparison of natural humic substances and synthetic ethylenediaminetetraacetic acid and nitrilotriacetic acid as washing agents of a heavy metal–polluted soil, J. Environ. Qual. 39 (2010) 855–862, https://doi.org/10.2134/jeq2009.0292.
[140] M.W.H. Evangelou, M. Ebel, A. Schaeffer, Chelate assisted phytoextraction of heavy metals from soil. Effect, mechanism, toxicity, and fate of chelating agents, Chemosphere 68 (2007) 989–1003, https://doi.org/10.1016/j.chemosphere.2007.01.062.
[141] Donald R. Burgess, N.I.S.T. SRD 46. Critically Selected Stability Constants of Metal Complexes, (2004). ⟨https://data.nist.gov/pdr/lps/ark:/88434/mds2-2154⟩ (accessed March 29, 2025).
[142] A.J. Hobson, D.I. Stewart, A.W. Bray, R.J.G. Mortimer, W.M. Mayes, M. Rogerson, I.T. Burke, Mechanism of vanadium leaching during surface weathering of basic oxygen furnace steel slag blocks: a microfocus X-ray absorption spectroscopy and electron microscopy study, Environ. Sci. Technol. 51 (2017) 7823–7830, https://doi.org/10.1021/ACS.EST.7B00874/ASSET/IMAGES/LARGE/ES-2017-00874W_0003.JPEG.
[143] A.J. Hobson, D.I. Stewart, A.W. Bray, R.J.G. Mortimer, W.M. Mayes, A.L. Riley, M. Rogerson, I.T. Burke, Behaviour and fate of vanadium during the aerobic neutralisation of hyperalkaline slag leachate, Sci. Total Environ. 643 (2018) 1191–1199, https://doi.org/10.1016/J.SCITOTENV.2018.06.272.
[144] S.E. Ziemniak, M.E. Jones, K.E.S. Combs, Solubility and phase behavior of Cr(III) oxides in alkaline media at elevated temperatures, J. Solut. Chem. 27 (1998) 33–66, https://doi.org/10.1023/A:1022688528380/METRICS.